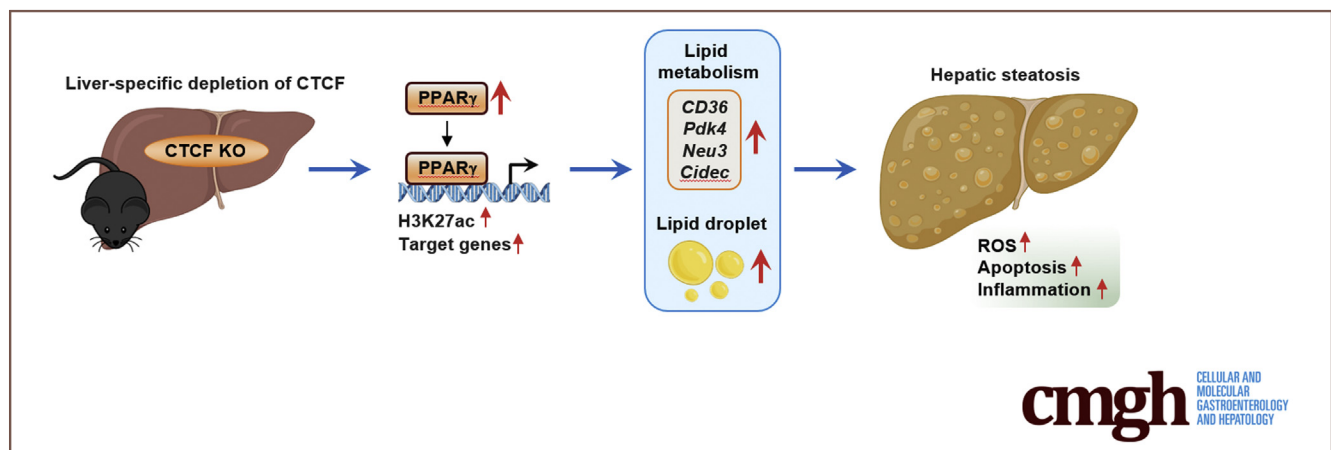


ORIGINAL RESEARCH

Liver-Specific Deletion of Mouse CTCF Leads to Hepatic Steatosis via Augmented PPAR γ Signaling

Yeeun Choi,^{1,2,*} Min-Ji Song,^{1,*} Woong-Jae Jung,^{1,3,*} Haengdueng Jeong,^{2,4} Seokjae Park,^{5,6} Bobae Yang,^{1,2} Eun-Chong Lee,^{1,2} Jung-Sik Joo,^{1,2} Dahee Choi,⁷ Seung-Hoi Koo,⁷ Eun-Kyoung Kim,^{5,6} Ki Taek Nam,^{2,4} and Hyoung-Pyo Kim^{1,2}

¹Department of Environmental Medical Biology, Institute of Tropical Medicine, ²Brain Korea 21 Plus Project for Medical Science, ³Department of Bioinformatics, Graduate School of Soongsil University, Seoul, Korea; ⁴Severance Biomedical Science Institute, Yonsei University College of Medicine, Seoul, Korea; ⁵Department of Brain and Cognitive Sciences, ⁶Neurometabolomics Research Center, Daegu Gyeongbuk Institute of Science and Technology, Daegu, Korea; ⁷Division of Life Sciences, Korea University, Seoul, Korea



SUMMARY

Liver-specific CCCTC-binding factor-deficient mice develop hepatic steatosis in a normal chow diet condition primarily through augmented peroxisome proliferator-activated receptor (PPAR) γ activity. Activated PPAR γ up-regulates its downstream target genes associated with lipid metabolic processes. Hepatic steatosis developed upon CCCTC-binding factor depletion is ameliorated by repression of PPAR γ .

BACKGROUND & AIMS: The liver is the major organ for metabolizing lipids, and malfunction of the liver leads to various diseases. Nonalcoholic fatty liver disease is rapidly becoming a major health concern worldwide and is characterized by abnormal retention of excess lipids in the liver. CCCTC-binding factor (CTCF) is a highly conserved zinc finger protein that regulates higher-order chromatin organization and is involved in various gene regulation processes. Here, we sought to determine the physiological role of CTCF in hepatic lipid metabolism.

METHODS: We generated liver-specific, CTCF-ablated and/or CD36 whole-body knockout mice. Overexpression or knock-down of peroxisome proliferator-activated receptor (PPAR) γ in

the liver was achieved using adenovirus. Mice were examined for development of hepatic steatosis and inflammation. RNA sequencing was performed to identify genes affected by CTCF depletion. Genome-wide occupancy of H3K27 acetylation, PPAR γ , and CTCF were analyzed by chromatin immunoprecipitation sequencing. Genome-wide chromatin interactions were analyzed by in situ Hi-C.

RESULTS: Liver-specific, CTCF-deficient mice developed hepatic steatosis and inflammation when fed a standard chow diet. Global analysis of the transcriptome and enhancer landscape revealed that CTCF-depleted liver showed enhanced accumulation of PPAR γ in the nucleus, which leads to increased expression of its downstream target genes, including fat storage-related gene *CD36*, which is involved in the lipid metabolic process. Hepatic steatosis developed in liver-specific, CTCF-deficient mice was ameliorated by repression of PPAR γ via pharmacologic blockade or adenovirus-mediated knock-down, but hardly rescued by additional knockout of *CD36*.

CONCLUSIONS: Our data indicate that liver-specific deletion of CTCF leads to hepatosteatosis through augmented PPAR γ DNA-binding activity, which up-regulates its downstream target genes associated with the lipid metabolic process. (*Cell Mol Gastroenterol Hepatol* 2021;12:1761–1787; <https://doi.org/10.1016/j.jcmgh.2021.07.016>)

Keywords: Liver Steatosis; CTCF; PPAR γ ; CD36.

The liver is the body's central hub for lipogenesis, fatty acid β -oxidation, and lipoprotein uptake and secretion. Dysregulation of these processes leads to various diseases, including fatty liver disease and liver cancer. Nonalcoholic fatty liver disease (NAFLD), characterized as an abnormal retention of excess lipid within hepatocytes (steatosis), is rapidly becoming a major health concern, with obesity and other metabolic syndromes increasing in prevalence worldwide. Although simple steatosis is relatively benign, it can develop into nonalcoholic steatohepatitis, along with hepatocyte injury, liver inflammation, and fibrosis. The physiologic and molecular machineries that cause NAFLD and trigger its progression to nonalcoholic steatohepatitis, however, remain poorly understood.¹

CCCTC-binding factor (CTCF) is a DNA binding protein with highly conserved 11 zinc finger domains that controls various aspects of gene expression, including transcription activation and repression, RNA splicing, chromatin insulation, genomic imprinting, and Variable(V), Diversity (D), and Joining (J) recombination.² Recent evidence has suggested that CTCF, along with cohesin proteins, mediates long-range chromatin interactions that contribute to the establishment of 3-dimensional genome organization. Research has shown that topological remodeling of the genome by CTCF can affect the expression of genes necessary for survival and differentiation in mammals and that CTCF mutations in human beings are associated with microcephaly and intellectual disability.³ Meanwhile, numerous studies have reported that genetically inducible CTCF knockout in specific cell types, including oocytes, lymphocytes, neurons, cardiomyocytes, and Langerhans cells, results in tissue-specific failure characterized by aberrant transcriptional dysregulation.⁴⁻¹² However, the precise role of CTCF in controlling liver metabolism *in vivo* remains poorly understood.

In this study, we used a conditional knockout (cKO) mouse system to show the role of CTCF in liver metabolism. Our results highlight an essential association between CTCF and liver steatosis and showed CTCF to be a crucial regulator of hepatic lipid homeostasis.

Results

Liver-Specific Deletion of CTCF Leads to Liver Steatosis

To investigate the physiological role of CTCF in the liver, we generated liver-specific CTCF cKO mice by crossing mice bearing floxed CTCF alleles (Ctcf^{fl/fl}) with mice in which Cre expression was under the control of albumin promoter. Depletion of endogenous CTCF in the liver was confirmed at the messenger RNA (mRNA) and protein levels (Figure 1A–C). At 8 weeks of age, the livers of cKO mice appeared paler than those of WT mice (Figure 2A), although body weight, liver weight, and epididymal fat weight were not significantly different between wild-type (WT) and cKO mice (Figure 1D–F). Oil Red O staining showed that all of the cKO mice (6 of 6) experienced accumulation of lipid droplets in the liver, whereas none (0 of 6) of the WT mice did

(Figure 2B). Consistent with this observation, hepatic total cholesterol (TC) and triglyceride (TG) levels were increased markedly in the cKO mice (Figure 2C). Meanwhile, significant decreases in serum TC and TG were noted in cKO mice (Figure 2D), suggesting that the uptake of lipids into the liver was increased owing to the loss of CTCF. However, hepatic secretion rates of TG were similar between WT and cKO mice administered injections of tyloxapol to inhibit lipoprotein lipase activity (Figure 2E). Further examination of lipid metabolism by quantifying individual fatty acids with mass spectrometry showed that levels of fatty acids, whether saturated, monounsaturated, or polyunsaturated, were increased significantly in cKO mice livers, compared with WT mice livers (Figure 2F). These data indicate that ablation of CTCF significantly accelerates hepatic fat accumulation and facilitates the development of liver steatosis at 8 weeks of age, even on a normal chow diet.


We also examined whether hepatic fat accumulation elicited by the loss of CTCF affects glucose metabolism. In doing so, we found that fasting glucose levels in the blood, as well as in the liver, were unaffected by CTCF deficiency (Figure 3A). In addition, glucose tolerance, insulin tolerance, and pyruvate tolerance test results showed no differences between cKO and control mice (Figure 3B–D). These data show that liver steatosis caused by CTCF deficiency does not lead to insulin resistance or glucose metabolic imbalance.

Hepatic CTCF Deficiency Causes Enhanced Hepatocellular Injury and Liver Inflammation

Next, we examined the extent of liver injury in cKO mice given that hepatic accumulation of fatty acids is known to be harmful to hepatocytes.¹³ H&E staining of liver sections showed significant increases in the number of hepatocytes with karyomegaly and binucleation in cKO livers (Figure 4A). Increased serum levels of alanine aminotransferase and aspartate aminotransferase in the cKO mice showed that CTCF depletion induced hepatotoxicity in the liver (Figure 4B). Furthermore, the number of apoptotic and cycling cells was increased significantly in the livers of cKO mice when assessed by cleaved caspase 3 (Figure 4C) and bromodeoxyuridine (BrdU) incorporation (Figure 4D),

*Authors share co-first authorship.

Abbreviations used in this paper: Ad-PPAR γ 2, adenoviral peroxisome proliferator-activated receptor γ 2; BrdU, bromodeoxyuridine; ChIP-seq, chromatin immunoprecipitation sequencing; cKO, conditional knockout mice; CTCF, CCCTC-binding factor; Ctcf^{fl/fl}, floxed CCCTC-binding factor alleles; HNF4 α , hepatocyte nuclear factor-4 α ; H3K27ac, H3K27 acetylation; IL, interleukin; mRNA, messenger RNA; NAFLD, nonalcoholic fatty liver disease; P, promoter; PPAR, peroxisome proliferator-activated receptor; qRT-PCR, quantitative reverse-transcription polymerase chain reaction; RNA-seq, RNA sequencing; ROS, reactive oxygen species; TAD, topologically associating domain; TC, total cholesterol; TG, triglyceride; TNF, tumor necrosis factor; WT, wild-type.

 Most current article

© 2021 The Authors. Published by Elsevier Inc. on behalf of the AGA Institute. This is an open access article under the CC BY-NC-ND license (<http://creativecommons.org/licenses/by-nc-nd/4.0/>).

2352-345X

<https://doi.org/10.1016/j.jcmgh.2021.07.016>

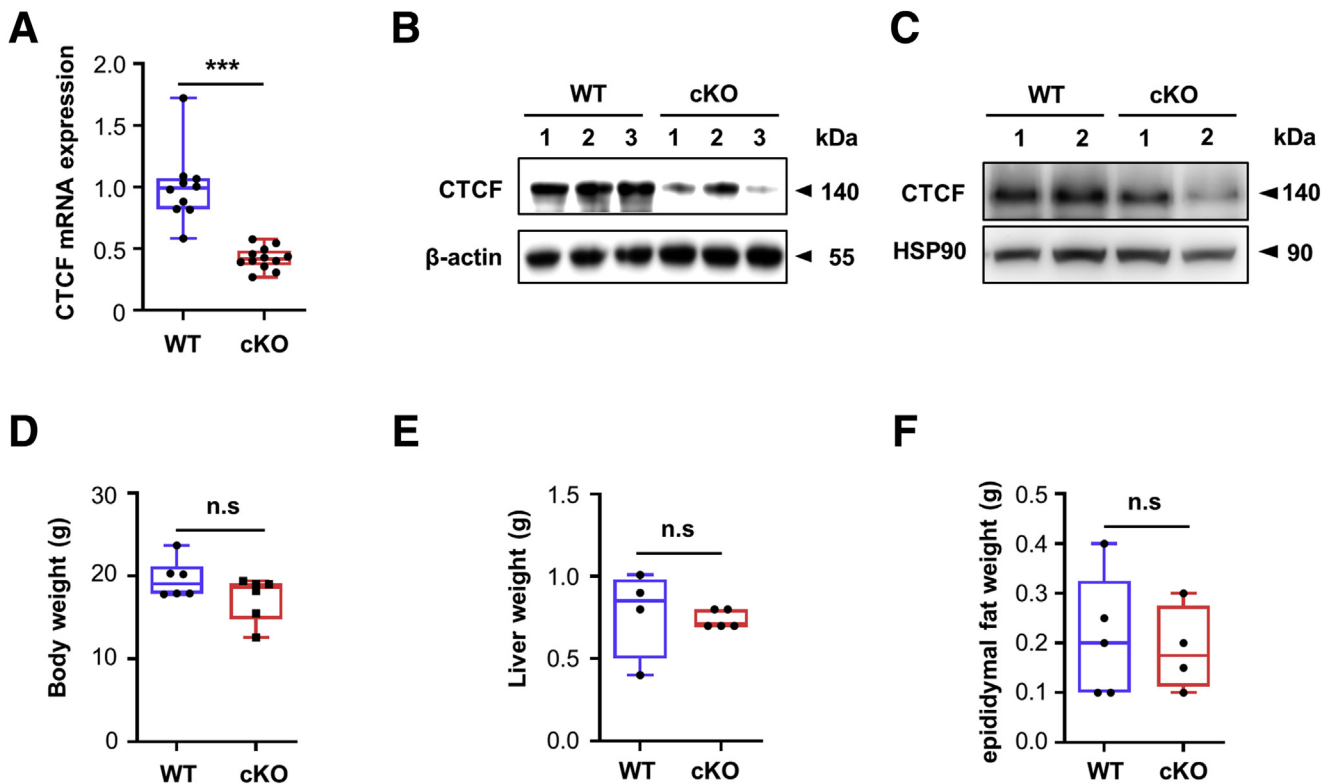


Figure 1. Depletion of endogenous CTCF in the livers of cKO mice. (A) qRT-PCR analysis was performed with total RNA isolated from livers from WT and cKO mice ($n = 6$ per group). (B and C) Immunoblotting was performed using total protein lysates extracted from (B) liver tissue or (C) primary hepatocytes using antibodies as indicated. (D) Body weight, (E) liver weight, and (F) epididymal fat weight of WT and cKO mice. *** $P < .001$, unpaired 2-tailed Student t test. HSP90, Heat Shock Protein 90.

respectively. Because increasing evidence has shown that reactive oxygen species (ROS) may be critical mediators of liver damage,¹⁴ we examined intracellular ROS production by flow cytometric analysis using 5-(and-6)-chloromethyl-2',7'-dichlorodihydrofluorescein diacetate acetyl ester (CM-H2DCFDA). The primary hepatocytes isolated from CTCF-depleted livers showed markedly higher ROS production than primary hepatocytes isolated from WT livers (Figure 5A). The hepatic population of F4/80^{high} Kupffer cells, which release proinflammatory cytokines and ROS, also were higher in CTCF-depleted livers (Figure 5B and C). In parallel with these results, quantitative reverse-transcription polymerase chain reaction (qRT-PCR) analyses showed that the expression of proinflammatory cytokines tumor necrosis factor (Tnf) α and interleukin (Il)1 β was increased significantly in CTCF-depleted livers, compared with WT livers (Figure 5D). In contrast, protein levels of TNF and IL1 β present in serum were very low and unaffected by CTCF deficiency (Figure 5E). Collectively, these data suggest that hepatic CTCF is essential to maintaining low levels of ROS and inflammation and that CTCF deficiency results in liver injury.

Increased Accumulation of PPAR γ Protein in the Nuclei of CTCF-Deficient Livers

To investigate the molecular mechanism of how CTCF deficiency affects lipid metabolism, we examined genome-

wide gene expression patterns by performing RNA sequencing (RNA-seq) analysis (Figure 6A). Differential RNA expression analysis showed 970 deregulated genes (adjusted $P < .05$; fold change, >2.0), 652 up-regulated and 318 down-regulated, upon CTCF depletion (Figure 6A). Gene ontology analysis indicated that the genes up-regulated by CTCF depletion were principally enriched for cell adhesion and many other development-related pathways, while the down-regulated genes were mostly associated with negative regulation of gluconeogenesis (Figure 7).

H3K27 acetylation (H3K27ac) is tightly coupled to epigenetic regulation of gene expression and marks both active promoters and enhancers. To investigate whether hepatic CTCF deficiency affects liver function via enhancer deregulation, we performed chromatin immunoprecipitation sequencing (ChIP-seq) analysis to compare genome-wide H3K27ac occupancies between WT and cKO livers ($n = 3$ per group) (Figure 6B). Differential H3K27ac regions were identified, with 1686 regions being hyperacetylated and 1917 regions being hypoacetylated, in cKO livers, compared with WT livers. De novo transcription factor binding motif analysis showed that hepatocyte nuclear factor-4 α (HNF4 α) motifs were enriched at hypoacetylated regions ($P = 10^{-16}$), while peroxisome proliferator-activated receptor (PPAR) motifs were enriched at hyperacetylated regions in CTCF-depleted livers ($P = 10^{-14}$) among others (Figure 6C). HNF4 α is

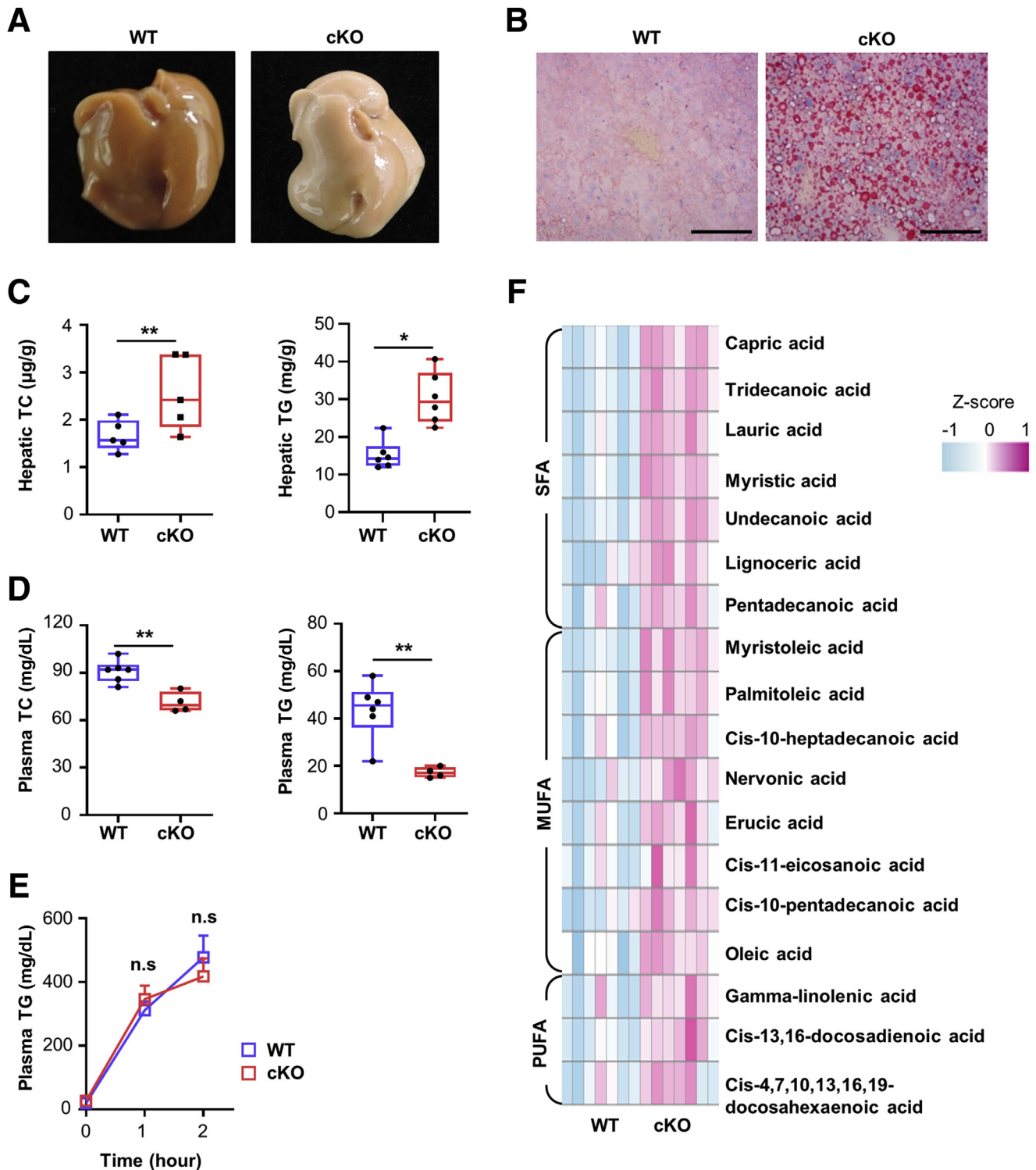


Figure 2. Mice with liver-specific CTCF knockout are susceptible to hepatic steatosis. (A) Macroscopic view of livers from WT and cKO mice at 8 weeks. (B) Representative images of histologic liver sections of WT and cKO mice stained with Oil Red O. Scale bar: 100 μm . (C and D) TC and TG levels in (C) liver and (D) serum from WT and cKO mice at 8 weeks ($n = 4\text{--}6$ per group). (E) Plasma TG levels at the indicated time points after injection of tyloxapol ($n = 5$ per group). The data are presented as the means \pm SD. (F) Mass spectrometric analysis of fatty acids from WT and cKO livers. The heat maps show fold differences between WT and cKO livers for saturated free fatty acid (SFA), monounsaturated fatty acid (MUFA), and polyunsaturated fatty acid (PUFA) ($n = 7$ per group). * $P < .05$, ** $P < .01$, unpaired 2-tailed Student t test.

known as a master regulator of hepatocyte-specific gene expression and to be essential for liver function. PPAR belongs to a class of nuclear receptors and plays a key role

in the transcriptional regulation of lipid metabolism in multiple tissues, including the liver. To further explore the cause of CTCF deficiency-induced hepatic fat

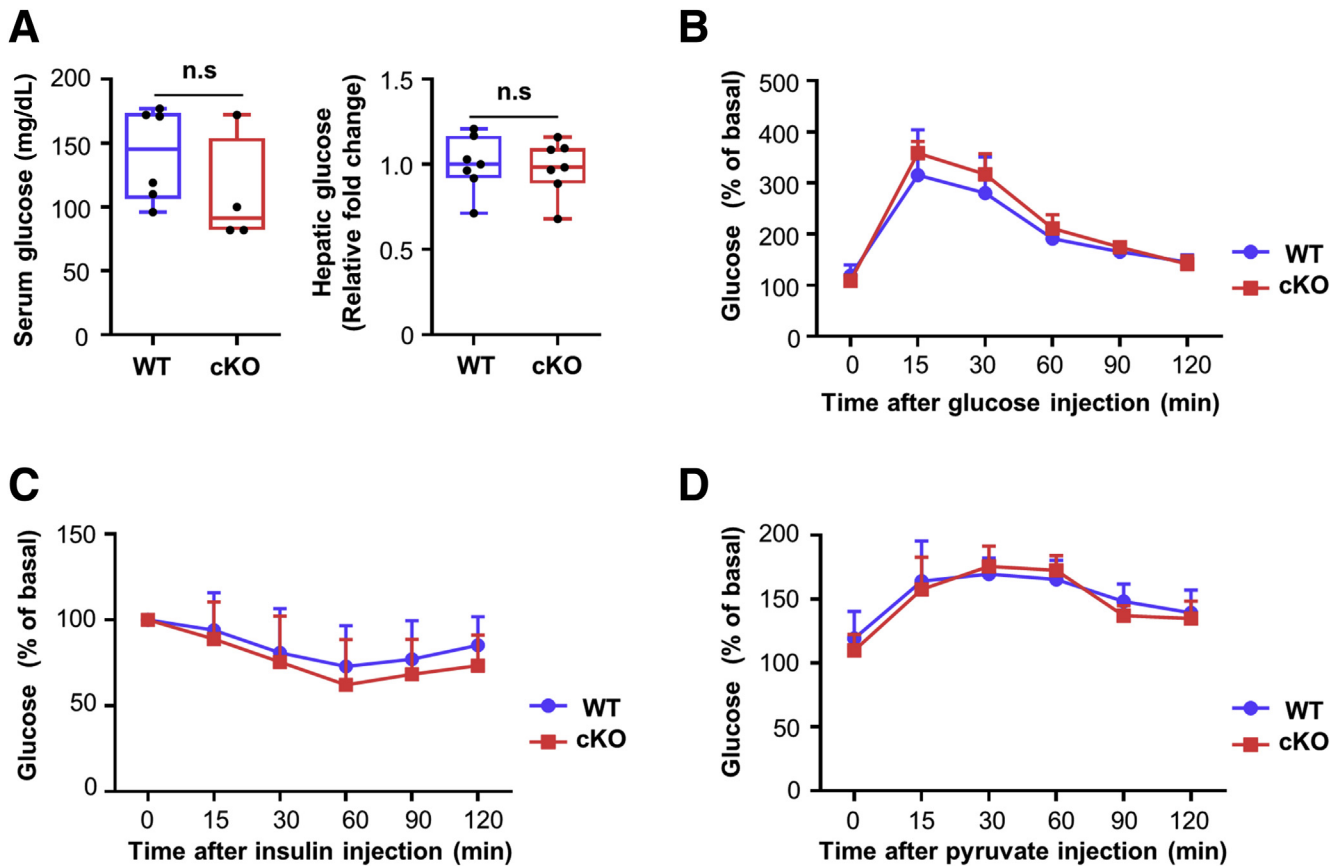


Figure 3. Normal glucose metabolism in liver-specific CTCF-knockout mice. (A) Glucose levels in serum (*left*) and liver tissue (*right*) from WT and cKO mice. (B–D) Percentage of starting plasma glucose concentrations during a (B) glucose tolerance test, (C) insulin tolerance test, and (D) pyruvate tolerance test in WT and cKO mice. The data are presented as the means \pm SD.

accumulation, we examined the expression of HNF4 α and PPAR transcription factors in cKO livers. qRT-PCR showed that CTCF depletion in the liver did not affect the expression of HNF4 α , PPAR α , or PPAR γ at the mRNA level (Figure 6D). However, PPAR γ protein levels were significantly higher in cKO livers than in WT livers, while protein levels of HNF4 α and PPAR α were similar (Figure 6E). We then examined subcellular distributions thereof and found that these transcription factors were mostly enriched in nuclear fractions (Figure 6F). Of note, nuclear enrichment of PPAR γ was significantly greater in CTCF-depleted livers than in WT livers (Figure 6F). These results suggest that CTCF deficiency in the liver is accompanied by enhanced accumulation of PPAR γ protein in the nucleus, which may affect global gene expression profiles by controlling enhancer landscapes.

Identification of PPAR γ Target Genes in CTCF-Deficient Livers

To gain insight into whether and how PPAR γ affects CTCF deficiency-induced liver steatosis, we explored genome-wide PPAR γ recruitment and its effect on gene expression. We first performed ChIP-seq to analyze the distribution of binding sites for PPAR γ in WT vs cKO livers.

Consistent with enhanced accumulation of PPAR γ in the nuclei of cKO livers, the number of PPAR γ binding sites, as well as the levels of PPAR γ occupancy, were increased markedly in CTCF-depleted livers, compared with WT livers (Figure 8A and B). Gene ontology analysis showed that the genes associated with PPAR γ peaks in both WT and cKO livers were mostly enriched in metabolism-related pathways (Figure 9). In addition, we analyzed differential enrichment of PPAR γ peaks and found that many more specific PPAR γ peaks were gained in cKO livers, while only a few peaks were lost in cKO livers, compared with WT livers ($n = 12,283$ vs 341, respectively) (Figure 8C). We then investigated genes associated with PPAR γ peaks gained in cKO livers ($n = 5683$), and differential RNA expression analysis for these genes showed 244 deregulated genes (adjusted $P < .05$; fold change, >2.0), 174 up-regulated and 70 down-regulated, upon CTCF depletion (Figure 8D). Gene set enrichment analysis showed that some of the differentially expressed PPAR γ target genes were enriched in cellular lipid metabolic processes (Figures 8E and F and 10). Among PPAR γ target genes, we found that the expression of CD36 was increased significantly in CTCF-depleted livers (Figure 8F and G). CD36 is a member of the class B scavenger-receptor family and shows fatty acid translocase activity. High expression of CD36 on the surface of a number

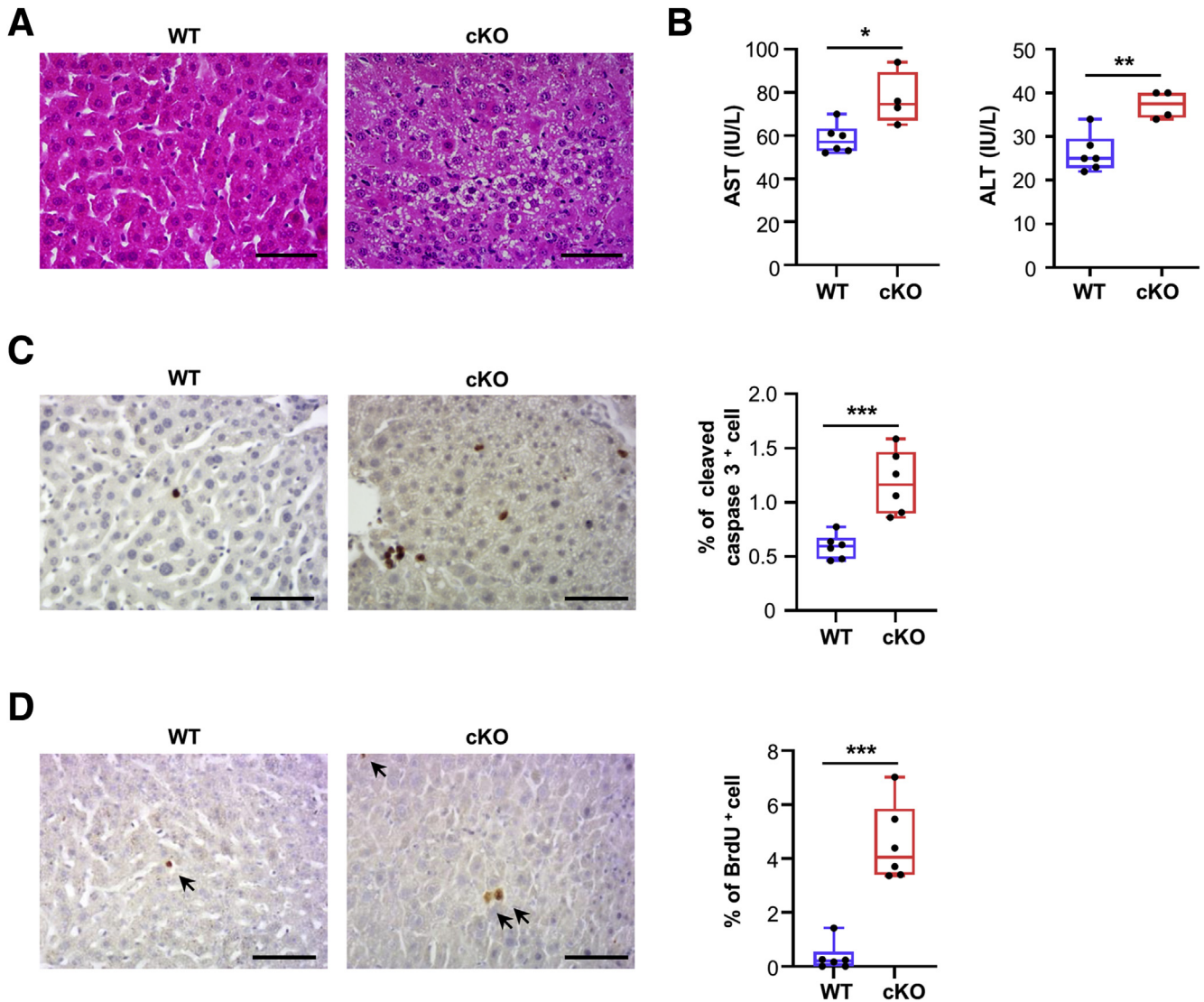


Figure 4. Enhanced injury, apoptosis, and proliferation in CTCF-deficient livers. (A) Representative images of histologic liver sections of WT and cKO mice at 8 weeks stained with H&E. Scale bar: 40 μ m. (B) Serum levels of alanine aminotransferase (ALT) and aspartate aminotransferase (AST) in WT and cKO mice. (C) Extent of hepatocyte apoptosis determined by staining of cleaved caspase-3 in WT and cKO mice. Scale bar: 40 μ m. Box plot indicates the percentages of cleaved caspase 3–positive cells. (D) Extent of cellular proliferation determined by BrdU labeling in WT and cKO mice. The arrows designated the location of BrdU⁺ cells. Scale bar: 40 μ m. Box plot indicates the ratio of BrdU-positive cells normalized to total hepatocytes in WT and cKO mice. n = 4–6 per group. * P < .05, ** P < .01, *** P < .001, unpaired 2-tailed Student t test.

of cell types, including muscle, adipose, and intestinal cells, is essential for lipid uptake, energy storage, and fat absorption, respectively. Basal expression of CD36 in normal hepatocytes is low, and overexpression of CD36 elicits hepatic fatty acid uptake and mediates liver steatosis. WT livers showed little enrichment for PPAR γ and H3K27ac in the *CD36* locus, which contains 3 promoters (P1–P3) (Figure 8G). In contrast, a regulatory region located between P1 and P2 showed enhanced PPAR γ occupancy, as well as increased H3K27ac levels, in cKO livers (Figure 8G), consistent with increased expression of *CD36* in cKO livers. Moreover, we detected marked enrichment of H3K4 trimethylation (H3K4me3), the most frequent histone modification found at active promoters (Figure 11A and C), at P3,

suggesting that the majority of CD36 transcripts in cKO livers originated from P3 (Figure 8G). There also was marked enrichment of H3K27ac near the P3 region and a corresponding depletion of the repressive histone mark H3K27 tri-methylation (H3K27me3) throughout the gene body region in cKO livers (Figures 8G and 11B and 11D). *PDK4* and *NEU3* genes, known to be involved in lipid metabolic processes and to be up-regulated in cKO livers, also were shown to be associated with enhanced PPAR γ occupancies and deregulated enhancer activity (Figure 12). These data show that enhanced PPAR γ activity mediated by CTCF depletion drives up-regulation of genes associated with lipid metabolic process, possibly via PPAR γ -mediated histone modifications.

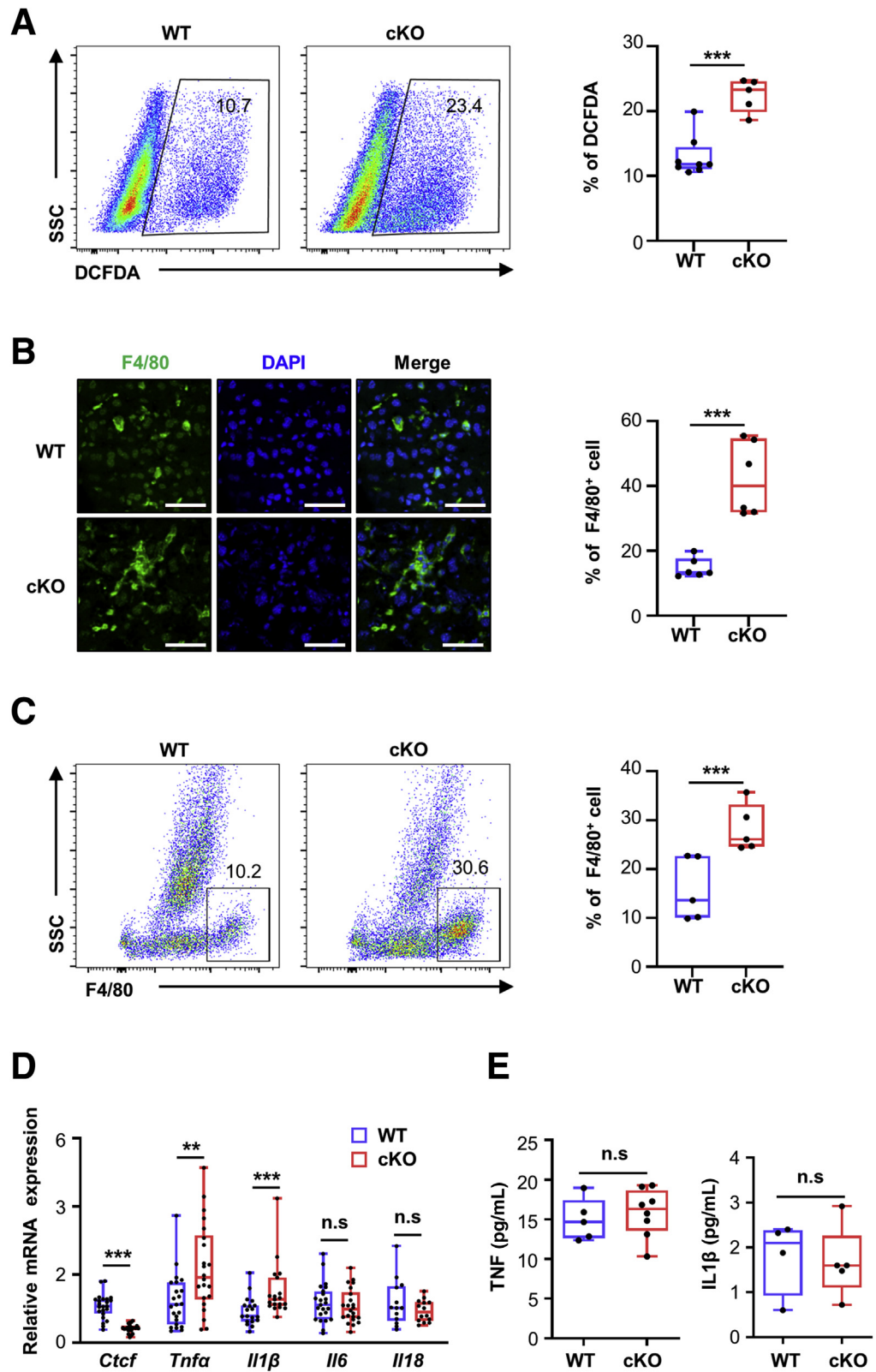


Figure 5. Hepatic CTCF deficiency causes liver inflammation. (A) Flow cytometric determination of ROS levels in primary hepatocytes isolated from WT and cKO mice. Box plot indicates the percentages of 2',7'-dichlorofluorescein diacetate (DCFDA)-positive cells (n = 5–8 per group). (B) Representative images of immunofluorescence for F4/80 (green) and 4',6-diamidino-2-phenylindole (DAPI) (blue). Scale bar: 50 μm. F4/80-positive cells were counted and indicated in the box plots (n = 6 per group). (C) Flow cytometric determination of Kupffer cells in the livers from WT and cKO mice. Box plot indicates the percentages of F4/80-positive cells (n = 5 per group). (D) mRNA expression of proinflammatory cytokine genes in the liver was determined by qRT-PCR (n = 19–20 per group). (E) Levels of TNF and IL1β cytokines in the serum of WT and cKO mice (n = 8 per group). **P < .01, ***P < .001, unpaired 2-tailed Student t test. SSC, Side Scatter.

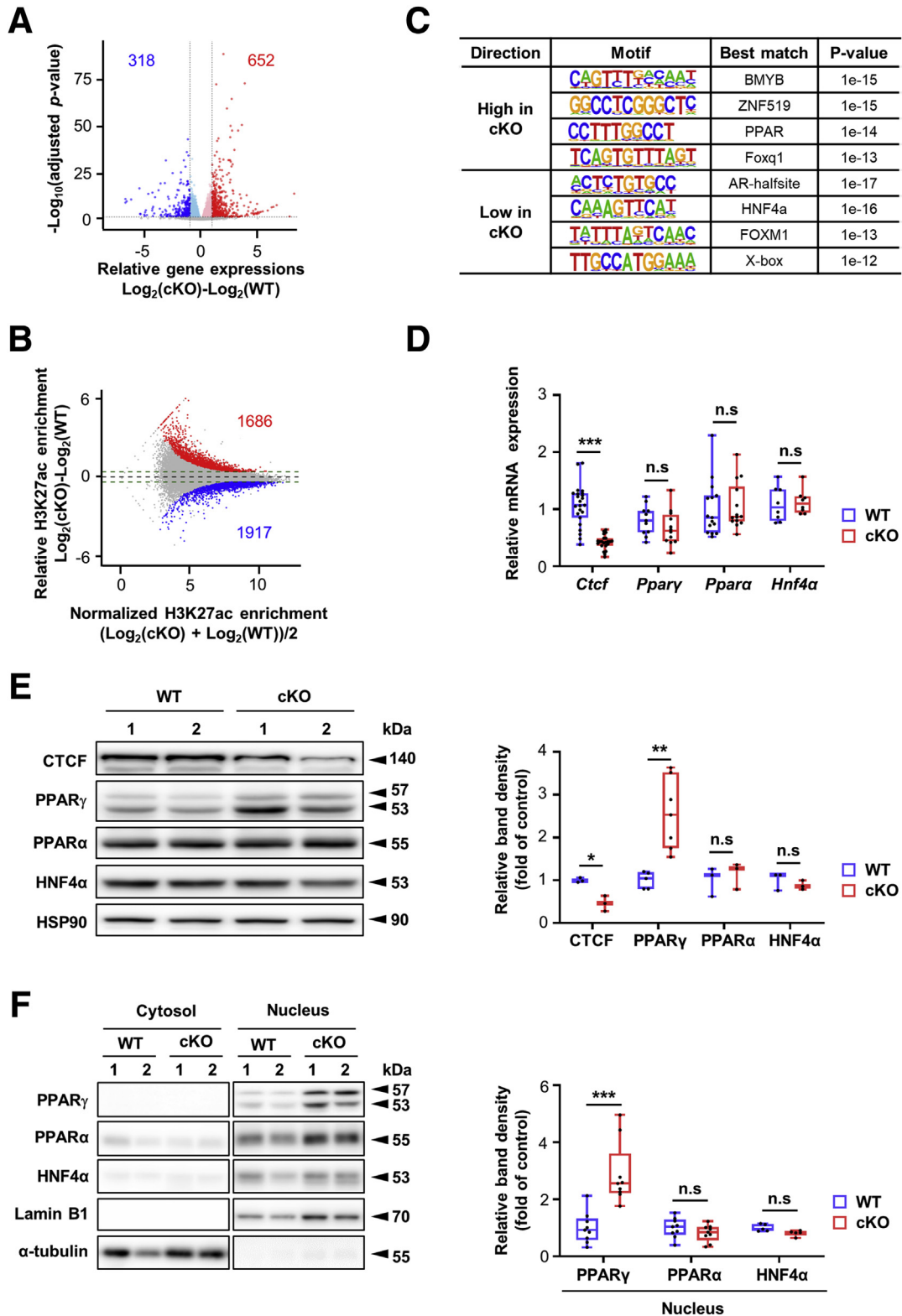
Pharmacologic Inhibition of PPARγ Affects CD36 Expression and Lipid Levels in CTCF-Deficient Livers

Further experiments with qRT-PCR showed that the mRNA levels of CD36 were increased in CTCF-depleted

livers (Figure 13A). Increased levels of CD36 protein also were shown in cKO livers by Western blot and immunofluorescence (Figure 13B and C). Flow cytometric analysis also showed that primary hepatocytes isolated from cKO livers contained higher levels of surface CD36 protein

(Figure 13D), as well as increased lipid accumulation, which was abrogated by pretreating the hepatocytes with sulfo-N-succinimidyl oleate, a chemical that binds irreversibly to CD36 and inhibits fatty acid uptake (Figure 13E).

To examine the contribution of PPAR γ to CTCF deficiency-induced increases in CD36, we treated primary hepatocytes with the PPAR γ inhibitor GW9662. Upon doing so, increased surface expression of CD36 protein, as



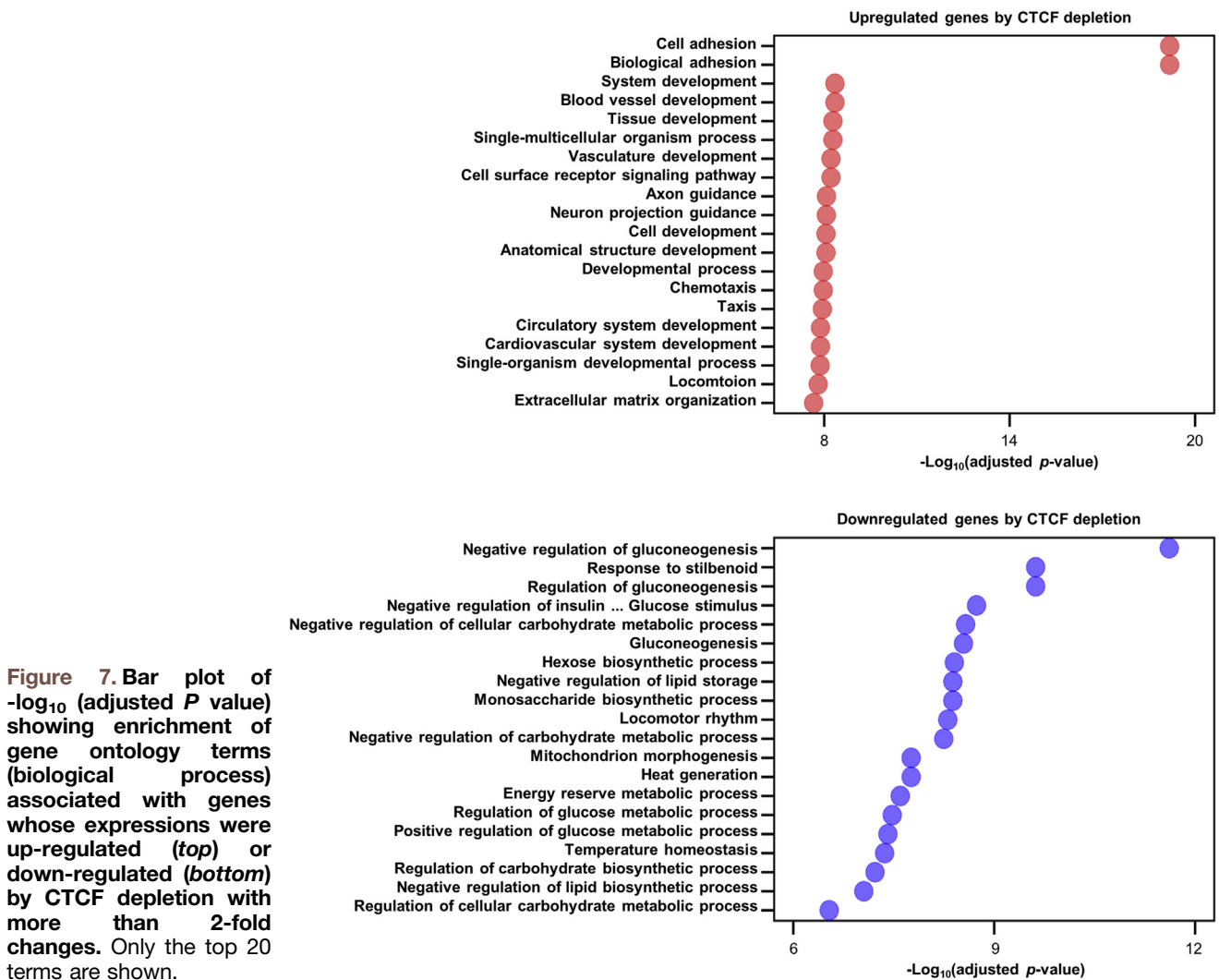


Figure 7. Bar plot of $-\log_{10}$ (adjusted P value) showing enrichment of gene ontology terms (biological process) associated with genes whose expressions were up-regulated (top) or down-regulated (bottom) by CTCF depletion with more than 2-fold changes. Only the top 20 terms are shown.

well as enhanced fatty acid uptake, in primary hepatocytes isolated from cKO livers were diminished by treatment with GW9662 in a dose-dependent manner (Figure 14A and B). To further examine the role of PPAR γ in liver steatosis induced by CTCF depletion, we injected the PPAR γ inhibitor GW9662 into 4-week-old male mice daily for 2 weeks. Higher expression of CD36 in cKO livers was reduced markedly by PPAR γ inhibition at mRNA and protein levels (Figure 14C and D). Moreover, we detected a decrease in hepatic TC and TG levels in cKO mice

treated with GW9662 (Figure 14E and F). Thus, inhibition of PPAR γ by GW9662 partially reversed up-regulation of CD36 and lipid accumulation in CTCF-depleted livers.

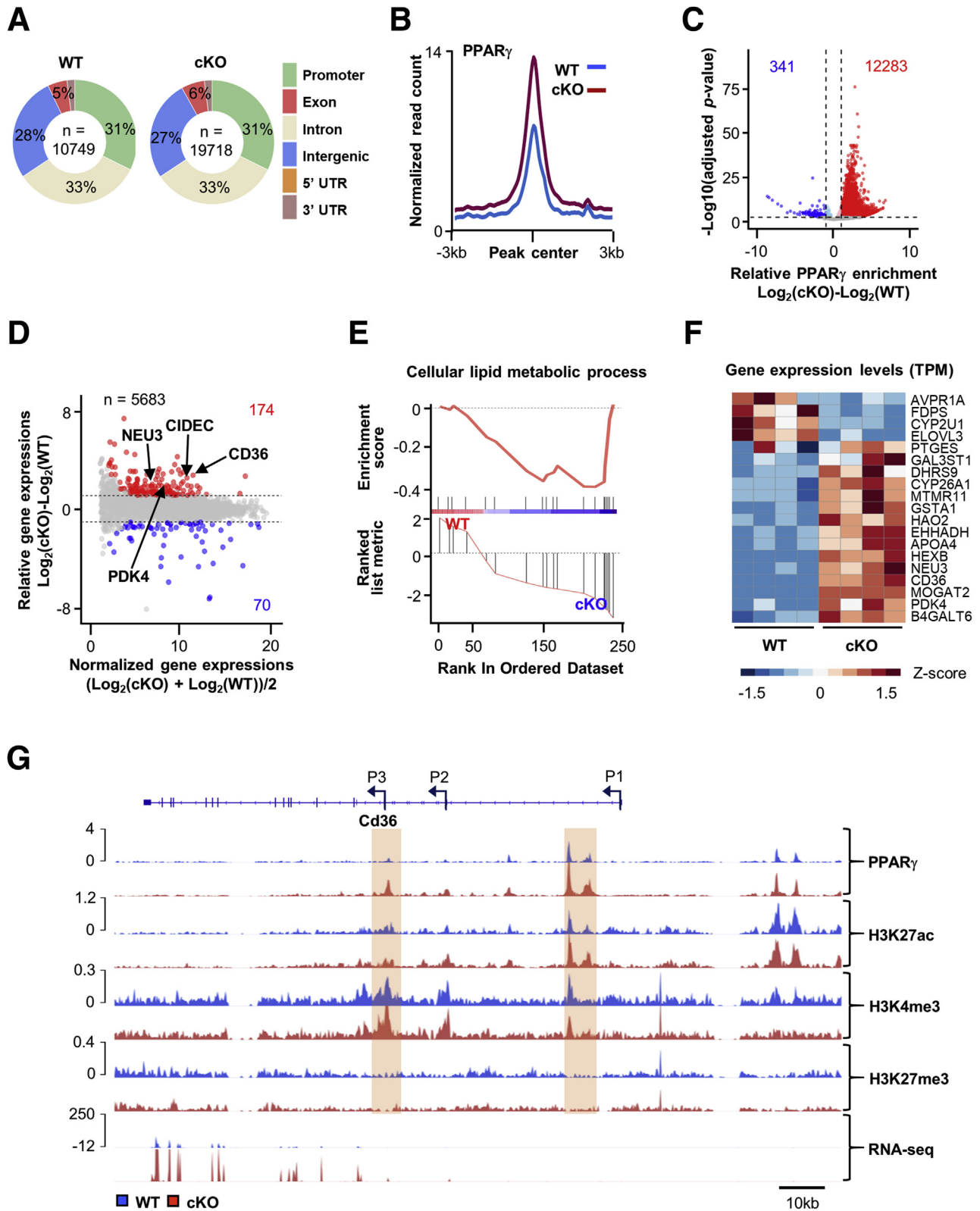
Effects of the Overexpression and Knockdown of PPAR γ in Hepatic Steatosis

Next, we investigated whether overexpression of PPAR γ can be a direct cause of liver steatosis by administering

Figure 6. (See previous page). Enhanced accumulation of PPAR γ protein in the nuclei of CTCF-deficient livers. (A) Volcano plot showing significant changes in genome-wide RNA expression between WT and cKO livers. The number of genes that showed greater than 2.0-fold increases in WT (blue) or cKO (red) livers with an adjusted P value of less than .05 is indicated. (B) MA plot showing differential enrichment of H3K27ac between WT and cKO livers. Differentially acetylated regions that showed greater than 1.3-fold increases in WT (lower) and cKO (upper) livers with an adjusted P value of less than .05 are indicated. (C) Enriched de novo motifs found by hypergeometric optimization of motif enrichment among differential H3K27ac regions. (D) Expression of PPAR γ , PPAR α , and HNF4 α mRNA was determined by real-time qRT-PCR ($n = 11-12$ per group). (E) Expression of CTCF, PPAR γ , PPAR α , HNF4 α , and HSP90 protein was determined by Western blot. (E) Right: The band densities of the proteins were quantified with HSP90 as the loading control and presented as box plots ($n = 7$ per group). (F) Western blot analysis of cytoplasmic and nuclear fractions of PPAR γ , PPAR α , and HNF4 α from WT and cKO livers. (F) The band densities of the nuclear proteins were quantified with Lamin B as the loading control and presented as box plots in the right panel ($n = 5-9$ per group). * $P < .05$, ** $P < .01$, *** $P < .001$, unpaired 2-tailed Student t test.

adenoviral PPAR γ 2 (Ad-PPAR γ 2) into wild-type mice via tail vein injections (Figure 15A-E). Ad-PPAR γ 2 injection induced the expression of PPAR γ and its downstream target gene *CD36* (Figure 15A and B), with higher levels of

hepatic TG and higher liver weights than control Ad-GFP mice (Figures 15C and 16A-C). Moreover, histologic analysis by H&E staining and Oil Red O staining showed the presence of numerous lipid droplets in the livers of Ad-



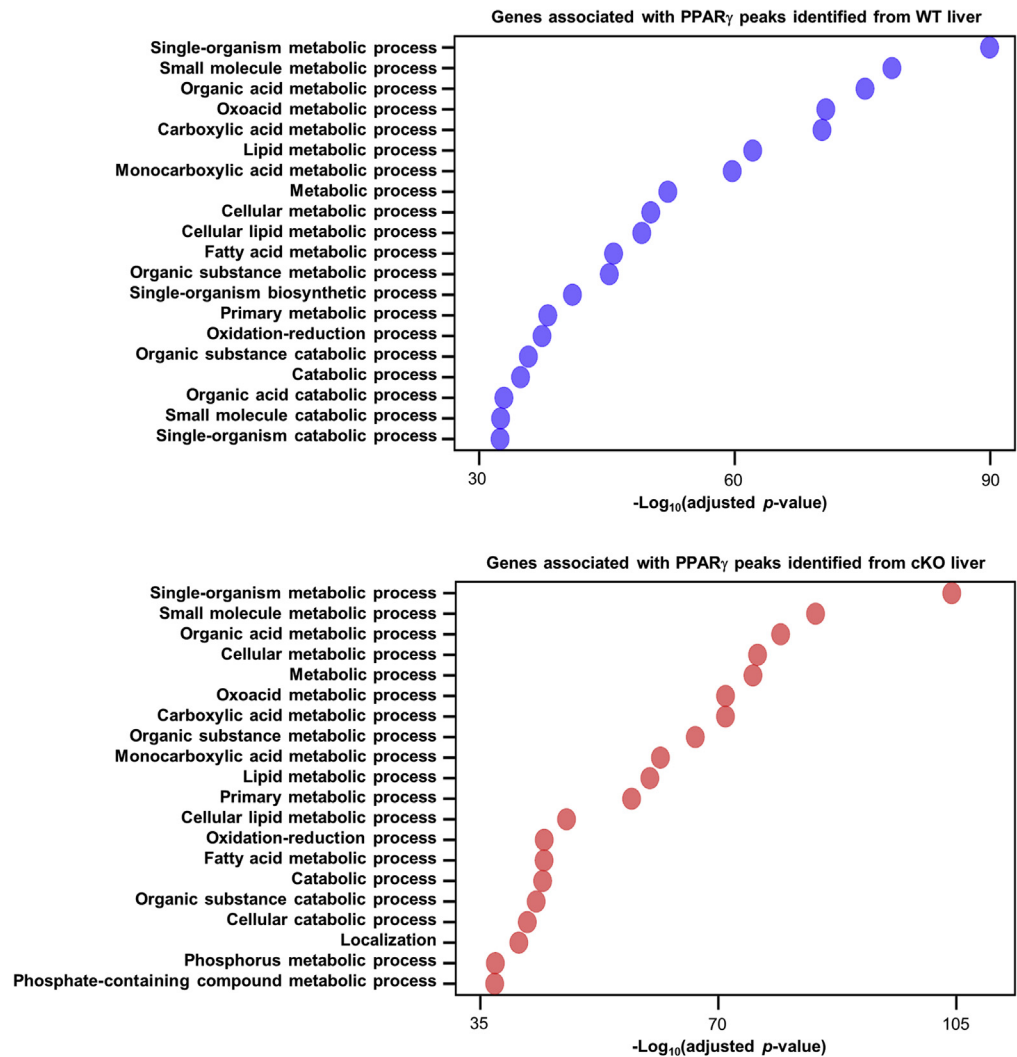


Figure 9. Bar plot of $-\log_{10}$ (adjusted P value) showing enrichment of gene ontology terms (biological process) for the genes whose expressions were associated with PPAR γ ChIP-seq peaks identified in WT (top) or cKO (bottom) livers. Only the top 20 terms are shown.

PPAR γ 2-injected mice (Figure 15D and E). These results suggest that hepatic overexpression of PPAR γ 2 results in severe hepatic steatosis, consistent with a previous report.¹⁵

To examine whether suppression of PPAR γ can reduce hepatic steatosis, liver-specific CTCF-deficient mice were administered adenovirus expressing either control (Ad-unspecified [Ad-US]) or PPAR γ short hairpin RNA via tail vein injections (Figure 15F–J). Expression of PPAR γ short hairpin RNA in the liver significantly reduced protein levels of

PPAR γ , as well as *CD36* (Figure 15F and G). Furthermore, cKO mice injected with Ad-shPPAR γ showed lower levels of hepatic TG (Figure H) and fewer lipid droplets (Figure 15I and J) than those injected with control Ad-US. Meanwhile, knockdown of PPAR γ in cKO livers did not change body or liver weights (Figure 16D–F). Taken together, these results indicate that activated PPAR γ signaling in CTCF-deficient livers plays a crucial role in the development of liver steatosis

Figure 8. (See previous page). Identification of PPAR γ -regulated genes in CTCF-deficient livers. (A) Pie charts showing the total numbers and genomic distributions of PPAR γ ChIP-seq peaks identified from WT and cKO livers. (B) Histogram showing the average tag density of PPAR γ ChIP-seq peaks. (C) Volcano plot showing significant changes in PPAR γ enrichment between WT and cKO livers. The number of peaks that showed greater than 2.0-fold increases in WT (blue) or cKO (red) livers with an adjusted P value of less than .05 is indicated. (D) RNA-seq MA plot for genes ($n = 5683$) associated with PPAR γ peaks ($n = 12,283$) gained in cKO livers. Mean abundance is plotted on the x-axis, and enrichment is plotted on the y-axis. The number of genes that showed more than 2.0-fold increases in WT (blue) or cKO (red) livers with an adjusted P value of less than .05 is indicated. (E) GSEA plot illustrating the enrichment of gene signatures for cellular lipid metabolic process. (F) Heatmap of RNA-seq signals for genes enriched in the cellular lipid metabolic pathway as shown in panel E. (G) Genomic snapshot of the *CD36* locus. Densities of ChIP-seq reads for PPAR γ , H3K27ac, H3K4me3, and H3K27me3 are shown. Densities of RNA-seq reads also are shown. Three known promoters (P1–P3) of *CD36* are indicated by arrows. TPM, transcripts per million; UTR, untranslated region.

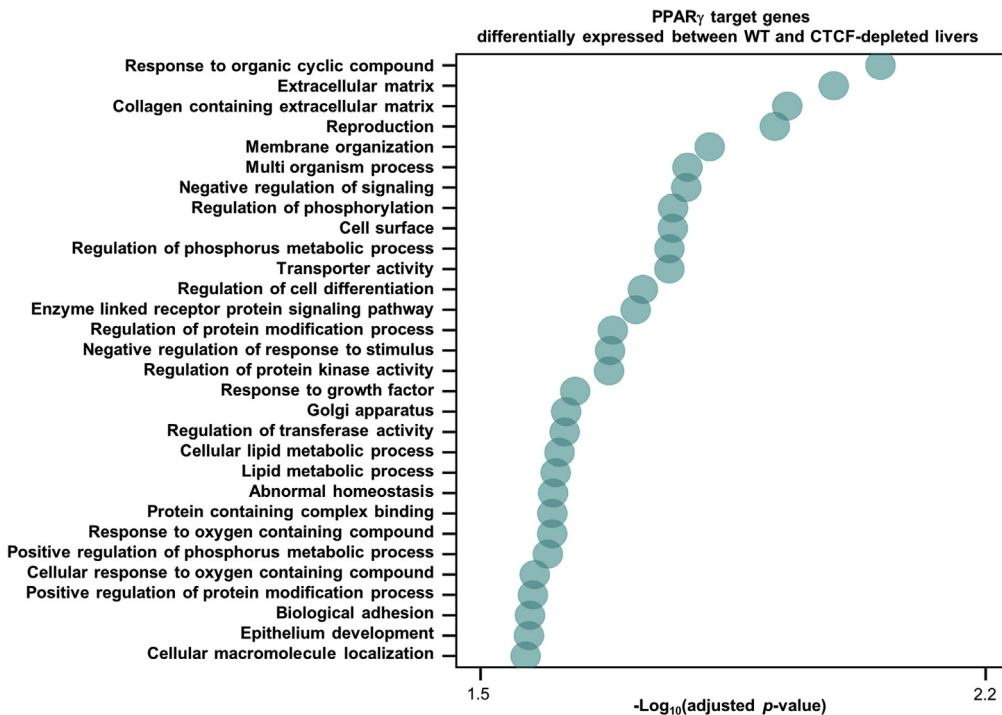


Figure 10. Functional enrichment analysis of PPAR γ target genes differentially expressed between WT and CTCF-depleted livers.

CD36 Knockout Is Not Enough to Rescue Hepatic Steatosis in CTCF-Deficient Mice

CD36 overexpression is well known to elicit hepatic fatty acid uptake and mediate liver steatosis. Given that CD36 expression is under the control of PPAR γ signaling, we examined whether CTCF deficiency-induced hepatic fat accumulation is attributable primarily to CD36 overexpression. We therefore crossed liver-specific CTCF conditional knockout (CTCF^{CKO}) mice with CD36 knockout (CD36^{CKO}) mice to generate double-knockout mice (CTCF^{CKO}/CD36^{CKO}). CD36 protein, overexpressed in CTCF-deficient (CTCF^{CKO}/CD36^{WT}) mice livers, clearly disappeared in double-knockout (CTCF^{CKO}/CD36^{CKO}) mice livers (Figure 17A). Hepatic TG levels, which were upregulated markedly in CTCF-deficient (CTCF^{CKO}/CD36^{WT}) mice, did not show any change with depletion of CD36 (CTCF^{CKO}/CD36^{CKO}) (Figure 17B). Histologic analysis by H&E staining and Oil Red O staining showed that the lipid accumulation seen in CTCF-deficient livers (CTCF^{CKO}/CD36^{WT}) was not diminished by additional depletion of CD36 (CTCF^{CKO}/CD36^{CKO}) (Figure 17C and D). These results showed that knockout of *CD36* alone is not enough to rescue hepatic steatosis in CTCF-deficient mice and that several PPAR γ downstream target genes may work together to contribute to the development of hepatic steatosis in a pleiotropic manner. Indeed, several PPAR γ target genes, such as *PDK4*, *NEU3*, and *CIDEA*, which have been reported to be associated with lipid metabolism, showed increased mRNA expression in CTCF-deficient livers, as well as CTCF/CD36 double-knockout livers, compared with WT livers (Figure 17E–G), further suggesting the coordinated contribution of multiple target genes.

Genome-Wide CTCF Occupancy and Higher-Order Chromatin Structure in cKO Livers

Given that CTCF is a well-known chromatin architectural protein and essential to organizing mammalian genomes, we examined genome-wide CTCF binding patterns by performing ChIP-seq (Figure 18A). CTCF occupancy was preferentially mapped at intergenic regions, as well as promoters and introns, in both WT and cKO livers (Figure 18B). Relatively modest levels of reduced CTCF enrichment was observed in cKO livers (Figure 18C and D), indicating that a significant amount of CTCF protein still was left in cKO livers (Figure 1B and C). Differential CTCF binding regions were identified, with 1178 regions being significantly lost in cKO livers, compared with WT livers (Figure 18E). The low-affinity binding sites were more sensitive to CTCF depletion in the decrease of CTCF occupancy than the high-affinity binding sites (Figure 18E). Integrated analysis of ChIP-seq for CTCF and H3K27ac showed little change in the enrichment of H3K27ac levels at the CTCF binding sites lost in cKO livers, indicating that loss of CTCF occupancy has little effect on enhancer activity at binding sites (Figure 18F).

We additionally performed in situ Hi-C to analyze higher-order chromatin structures in cKO livers (Figure 18G–M). Contact maps (Figure 18G) and compartment signals (Figure 18H–J) showed that segregation of active and inactive chromosome domains into A and B compartments was not altered significantly with CTCF depletion. We also examined topologically associating domains (TADs) using insulation scores and found that TAD numbers were quite similar between WT and cKO livers (Figure 18K). Moreover, the capacity of preventing inter-TAD interactions was decreased only slightly in cKO

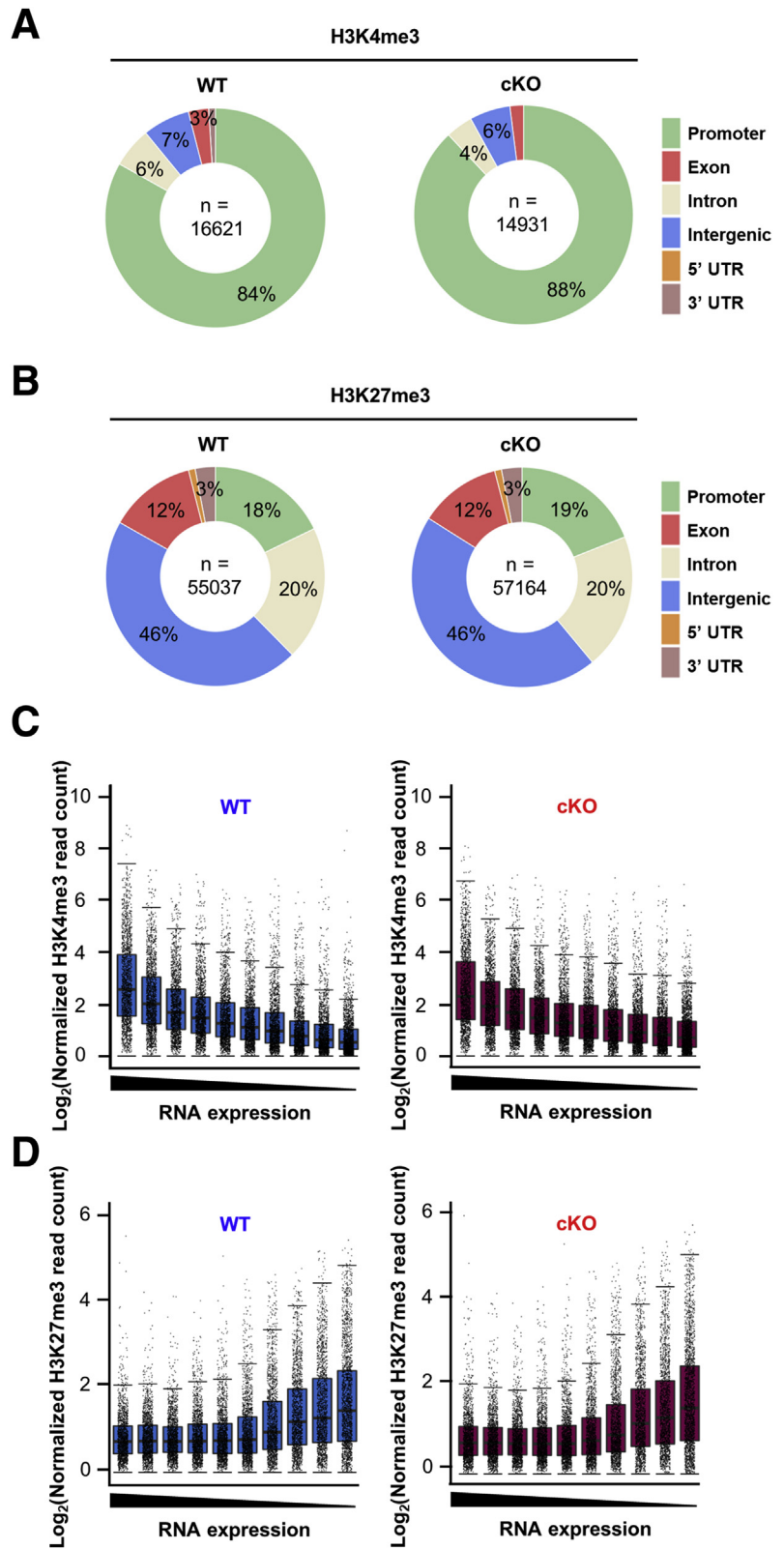


Figure 11. CHIP-seq analysis for H3K4me3 and H3K27me3. (A and B) Pie charts showing the total numbers and genomic distributions of (A) H3K4me3 and (B) H3K27me3 ChIP-seq peaks identified from WT (left) and cKO (right) livers. (C and D) Boxplots showing the relative levels of (C) H3K4me3 or (D) H3K27me3 for genes categorized according to mRNA expression in WT (left) and cKO (right) livers. UTR, untranslated region.

livers (Figure 18L and M), and we noted little changes in genome-wide intra-TAD chromatin interactions (Figure 18N). These data suggest that 3-dimensional

genome organization, as reflected in compartments and TADs, still was preserved in cKO livers, possibly owing to significant amounts of residual CTCF protein, most of

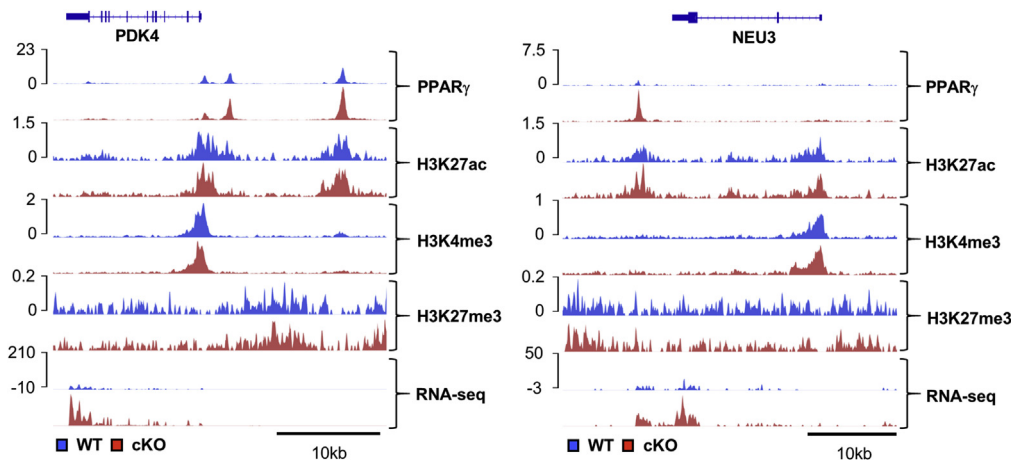


Figure 12. Identification of differentially expressed PPAR γ target genes upon CTCF depletion. Genomic snapshot of the *PDK4* (left) and *NEU3* (right) loci. Densities of ChIP-seq reads for PPAR γ , H3K27ac, H3K4me3, and H3K27me3 are shown. Densities of RNA-seq reads also are shown.

which is thought to bind preferentially to high-affinity binding sites forming TAD boundary elements.

Discussion

CTCF is a versatile transcriptional regulator and chromatin architectural protein required for mammalian development and for cellular differentiation of various lineages; however, its function in the liver is poorly understood.^{4–12} Our genetic analysis of CTCF in a liver-specific knockout mouse model indicated that it is essential for maintaining homeostasis of hepatic lipid metabolism.

PPAR γ , which is implicated in the development of many metabolic diseases, can bind various free fatty acids to control the transcription of many genes governing lipid metabolism.¹⁶ Although PPAR γ is found at low levels in normal liver, increased expression of PPAR γ is a general property of steatotic liver.^{17–20} Consistent with these previous reports, our H3K27ac ChIP-seq analysis, followed by de novo transcription factor binding motif analysis, highlighted the PPAR binding motif as being highly enriched in activated enhancer regions in CTCF-depleted livers. Moreover, we observed increased accumulation of PPAR γ in the nuclei of CTCF-deficient livers that seemed to be regulated by post-translational modifications, such as phosphorylation, ubiquitination, and small ubiquitin-like modifier (SUMO) conjugation (or SUMOylation),^{21,22} given that mRNA levels of PPAR γ were comparable between WT and cKO livers. Augmented PPAR γ activity in cKO livers also was indicated by significant increases in PPAR γ DNA binding in vivo, leading to increased expression of its downstream target genes involved in lipid metabolic processes. The crucial role of PPAR γ in the development of hepatic steatosis in CTCF-depleted mice was validated further by gain-of-function and loss-of-function experiments. Adenoviral overexpression of PPAR γ 2 in WT mice resulted in accumulation of hepatic TG and lipid droplets. In contrast, repression of PPAR γ , by both pharmacologic inhibition and adenovirus-mediated knockdown, significantly decreased liver TG contents with a lessening of hepatic steatosis developed in CTCF-deficient mice.

One of the major PPAR γ target genes up-regulated in CTCF-deficient livers is *CD36*, which facilitates fatty acid transport, allowing for the accumulation of lipids in the liver. *CD36* has been reported previously to have a role in intestinal fat absorption, lipid storage in adipose tissue, and lipid utilization by cardiac and skeletal muscle.^{23–28} Although basal expression of *CD36* in the liver is very low and although *CD36* does not play a major role in fatty acid uptake in normal liver, recent findings have suggested a causative role for *CD36* in the pathogenesis of hepatic steatosis. For example, increased hepatic *CD36* expression has been observed in various pathologic conditions, including NAFLD and type 2 diabetes mellitus.^{29–31} Moreover, forced expression of *CD36* by adenovirus-mediated infection was found to increase hepatic fatty acid uptake and triglyceride storage, and disruption of hepatic *CD36* was shown to attenuate fatty liver in high-fat-diet-fed mice.^{32–35} Consistent with these previous reports, we also discovered that hepatic fatty acid uptake enhanced in CTCF-null primary hepatocytes was down-regulated after treatment with a *CD36* inhibitor, sulfo-N-succinimidyl oleate.

Many studies have shown that PPAR γ regulates *CD36* expression via binding to a PPAR γ -responsive element in the proximal region of the *CD36* promoter and that both natural and synthetic PPAR γ ligands, including prostaglandin J2 and thiazolidinediones, can increase *CD36* expression.^{36–38} In WT livers in which expression of *CD36* is very low, we found near-baseline levels of H3K27ac and PPAR γ at the *CD36* locus. However, significant increases in *CD36* expression induced by loss of CTCF was accompanied by increased binding of PPAR γ to several enhancer regions of the *CD36* locus, with increased occupancies of active histone marks H3K27ac and H3K4me3, but decreased levels of the repressive histone mark H3K27me3. *CD36* may exploit a feed-forward cycle to positively influence its own de novo synthesis by facilitating the entry of fatty acids, which can function as a ligand of PPAR γ to activate PPAR γ -mediated transcription of *CD36*.

The essential role of PPAR γ in *CD36* expression was verified by experiments showing that treatment of the PPAR γ antagonist GW9662, as well as adenovirus-mediated PPAR γ knockdown, in the CTCF-deficient mice significantly

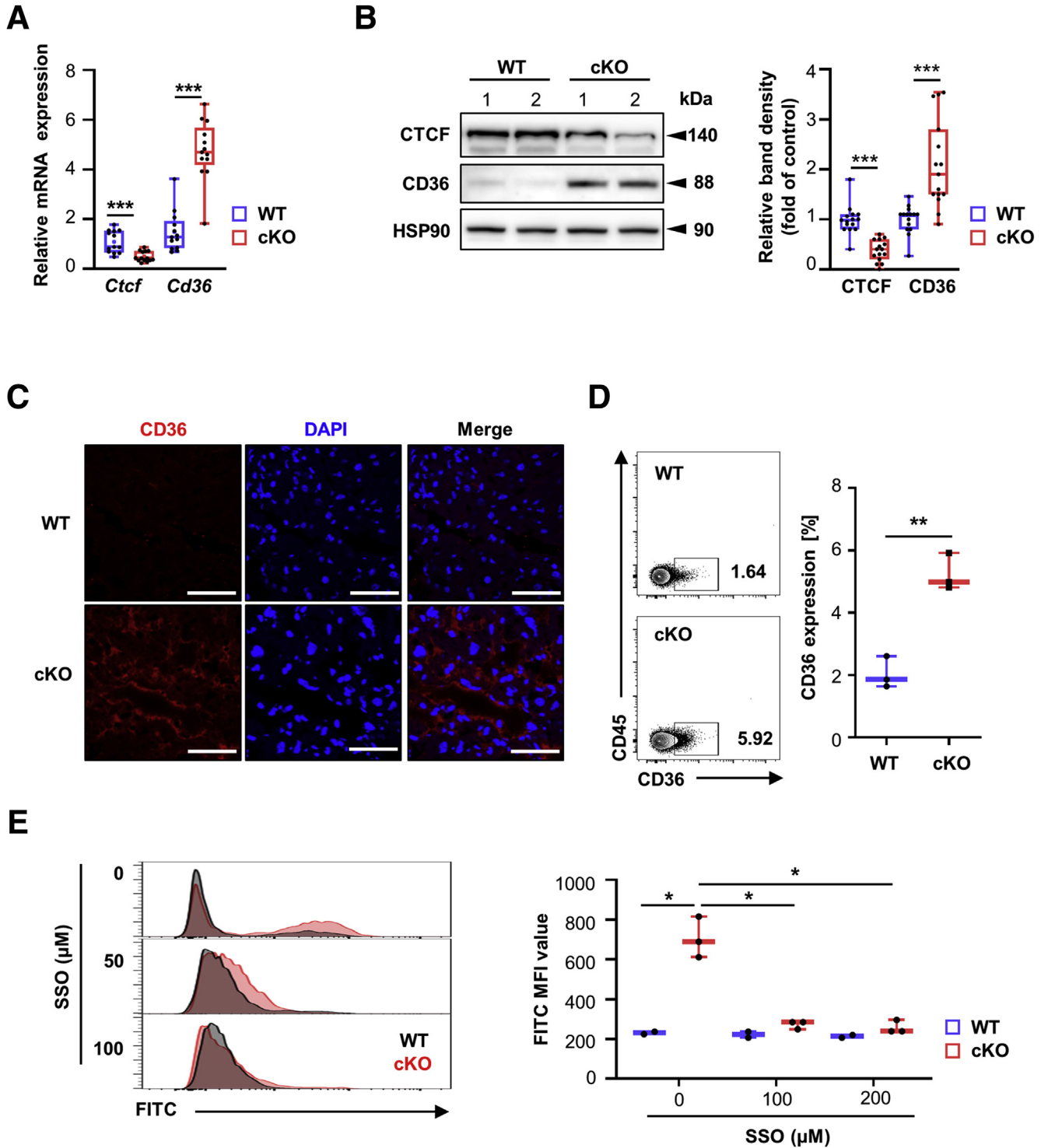
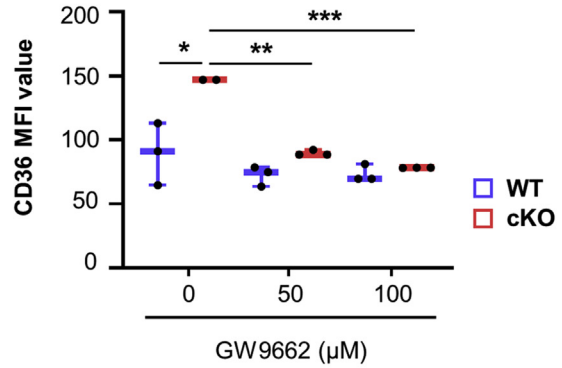
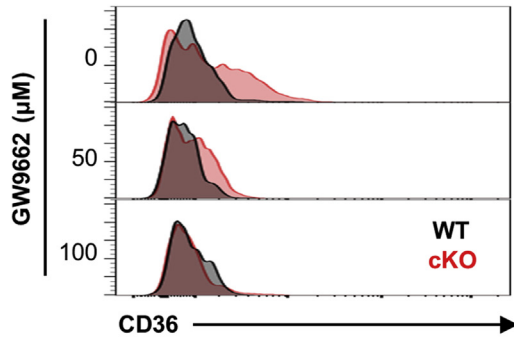
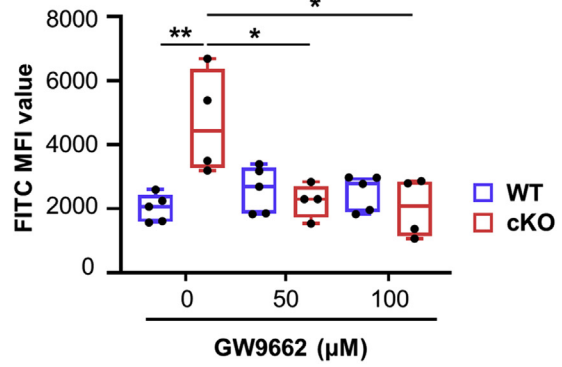
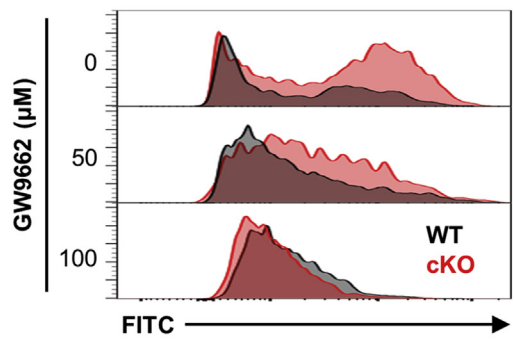


Figure 13. Increased CD36 expression and fatty acid uptake in CTCF-deficient liver. (A and B) Expression of CD36 (A) mRNA (n = 13–14 per group) and (B) protein (n = 15 per group) in livers from WT and cKO mice was determined by real-time qRT-PCR and Western blot, respectively. *Right:* The band densities of the proteins were quantified and presented as box plots. (C) Representative immunofluorescence staining for CD36 (red) and 4',6-diamidino-2-phenylindole (DAPI) (blue) in livers from WT and cKO mice. *Scale bar:* 50 μ m. (D) CD36 expression levels in primary hepatocytes from WT and cKO mice were assessed by flow cytometry (n = 3 per group). (E) Uptake of fatty acid by primary hepatocytes was determined by flow cytometry in the absence or presence of sulfo-N-succinimidyl oleate (SSO) at the indicated concentrations. Cells were gated for fluorescence-tagged fatty acid and indicated in the box plots (n = 3 per group). **P* < .05, ***P* < .01, ****P* < .001, unpaired 2-tailed Student *t* test. FITC, Fluorescein; HSP90, Heat shock protein 90; MFI, Mean Fluorescent Intensity.

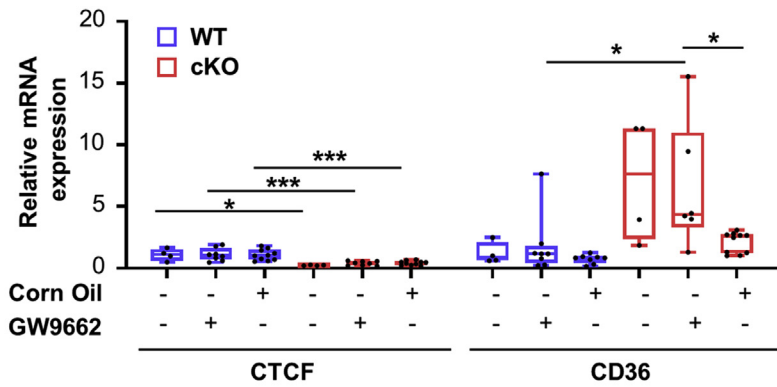
A



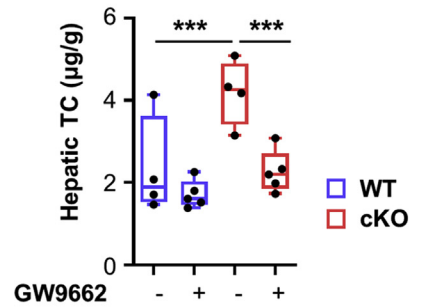
B



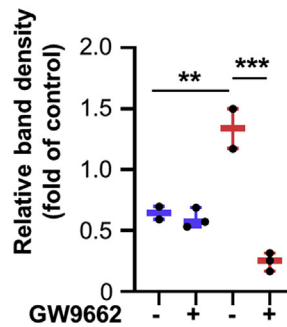
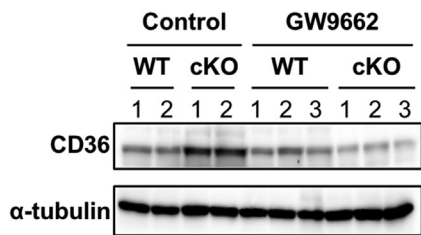
C



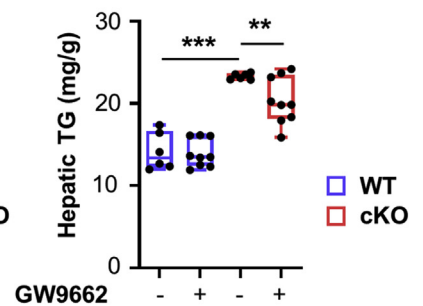
E



D



F



decreased hepatic CD36 expression. Because GW9662 was clearly able to repress fatty acid transport activity in CTCF-deficient primary hepatocytes, we wondered whether blocking CD36 could ameliorate hepatic steatosis developed as a result of CTCF depletion. However, introduction of CD36 depletion to liver-specific CTCF knockout mice elicited only modest changes in hepatic accumulation of lipid droplets, suggesting additional gene sets regulated by PPAR γ may pleiotropically contribute to the development of hepatic steatosis. Indeed, the PPAR γ target genes differentially expressed between WT and cKO livers regulate various aspects of lipid metabolism: For example, cell death-inducing DFFA-like effector c, a lipid droplet-associated protein that promotes intracellular triglyceride storage, was highly up-regulated in cKO livers (Figure 8D), consistent with other studies of genetic or diet-induced hepatosteatosis.³⁹ PDK4, recently reported to control hepatic steatosis in a mouse model by regulating expression of genes related to fatty acid uptake and synthesis,⁴⁰ showed increased PPAR γ occupancy at the enhancer region, which may drive up-regulation of its expression in CTCF-deficient livers (Figure 12). Plasma membrane-associated sialidase, NEU3, the overexpression of which is known to increase hepatic TG accumulation and enhance hepatic PPAR γ protein levels,⁴¹ was another PPAR γ target up-regulated in cKO livers (Figure 12). Further analysis in the future would be required to address how PPAR γ target genes are coordinated to regulate the development of hepatic steatosis in CTCF-deficient livers.

It is well known that CTCF is essential in mediating chromatin folding into TADs. However, substantial defects in TAD insulation are observed only when CTCF is almost completely depleted. Indeed, research has shown that RNA interference-mediated knockdown of CTCF elicits much milder defects in TAD folding compared with acute and near-complete depletion of endogenous CTCF, using the auxin-inducible degron system.^{42,43} Given the insufficient depletion of CTCF in cKO liver, which seems to be enough to maintain TAD organization, it is not likely that defects in higher-order chromatin organization at the resolution of TADs causes hepatic steatosis.

The triggering of hepatic steatosis in liver-specific CTCF-null mice may result from hepatocyte injury and liver inflammation.⁴⁴ Injured hepatocytes might release damage-associated molecular patterns that can stimulate Kupffer cells to release proinflammatory cytokines. Overaccumulation of lipid toxicity also has been shown to facilitate the generation of lipotoxic metabolites and ROS that might contribute to cell death and compensatory cell proliferation.^{45–48} Although mitochondrial dysfunction often is associated with increased ROS production, loss of CTCF in the liver does not lead to alterations in mitochondria

morphology, mitochondrial membrane potential, or respiration function (data not shown). The increased activation of Kupffer cells and enhanced production of ROS can lead to further progression of NAFLD to nonalcoholic steatohepatitis.

In summary, we discovered that liver-specific CTCF-deficient mice develop hepatic steatosis in a normal chow-diet condition primarily through augmented PPAR γ activity that modulates genome-wide enhancer landscapes to up-regulate target genes associated with hepatic lipid metabolism.

Methods

Mice

Mice carrying a conditional CTCF allele (Ctcf^{f/f}) were described in our previous study.⁴ To generate mice with conditional deletion of CTCF in the liver, Ctcf^{f/f} mice were bred with mice expressing Cre recombinase driven by an albumin promoter (Alb-cre; Jackson Laboratory, Bar Harbor, ME).⁴⁹ Alb-cre mice were kindly provided by Han-Woong Lee (Yonsei University, Seoul, Korea). Ctcf^{f/f} littermate mice were used as WT controls throughout the study. CD36 knockout mice⁵⁰ were purchased from Jackson Laboratory and bred with liver-specific conditional CTCF knockout mice (Alb-cre/Ctcf^{f/f}) to generate double-knockout mice for CTCF and CD36 (Alb-cre/Ctcf^{f/f}/CD36KO). All experiments were performed on 8- to 20-week-old male mice fed with a standard chow diet after an overnight fast. All mouse experimental procedures were approved by the Department of Laboratory Animal Resources Committee of Yonsei University College of Medicine.

Chemical Inhibitors

Sulfosuccinimidyl oleate (Cayman Chemical, Ann Arbor, MI) stock was prepared in 100% dimethyl sulfoxide, and GW9662 (Sigma-Aldrich, St. Louis, MO) stock was prepared in corn oil and diluted to indicated concentrations for in vitro and in vivo experiments.

Preparation of Recombinant Adenovirus

Adenovirus-expressing PPAR γ 2 was generated through homologous recombination between a linearized transfer vector pAD-Track and the adenoviral backbone vector pAD-Easy as described previously.⁵¹ Adenovirus for Green fluorescent protein (GFP) only was described previously.⁵² Adenovirus expressing unspecific RNA interference (US) and PPAR γ RNA interference were described previously.⁵³

Histologic Analysis

A cross-section of the left lateral lobe of the liver was fixed in 4% paraformaldehyde at room temperature. The

Figure 14. (See previous page). **Pharmacologic inhibition of PPAR γ decreases hepatic lipid levels in CTCF-deficient mice.** (A and B) Primary hepatocytes were treated with dimethyl sulfoxide or GW9662 for 24 hours, and (A) levels of CD36 expression (n = 3 per group) and (B) uptake of fatty acid (n = 3 per group) were quantified by flow cytometry. (C–F) Mice were injected with GW9662 (100 μ M) daily for 2 weeks. Expression of CD36 (C) mRNA (n = 13–14 per group) and (D) protein (n = 4–10 per group) was determined by real-time qRT-PCR and Western blot, respectively. (E) TC and (F) TG levels in livers (n = 3 per group). **P* < .05, ***P* < .01, ****P* < .001, unpaired 2-tailed Student *t* test. FITC, Fluorescein; MFI, Mean Fluorescent Intensity.

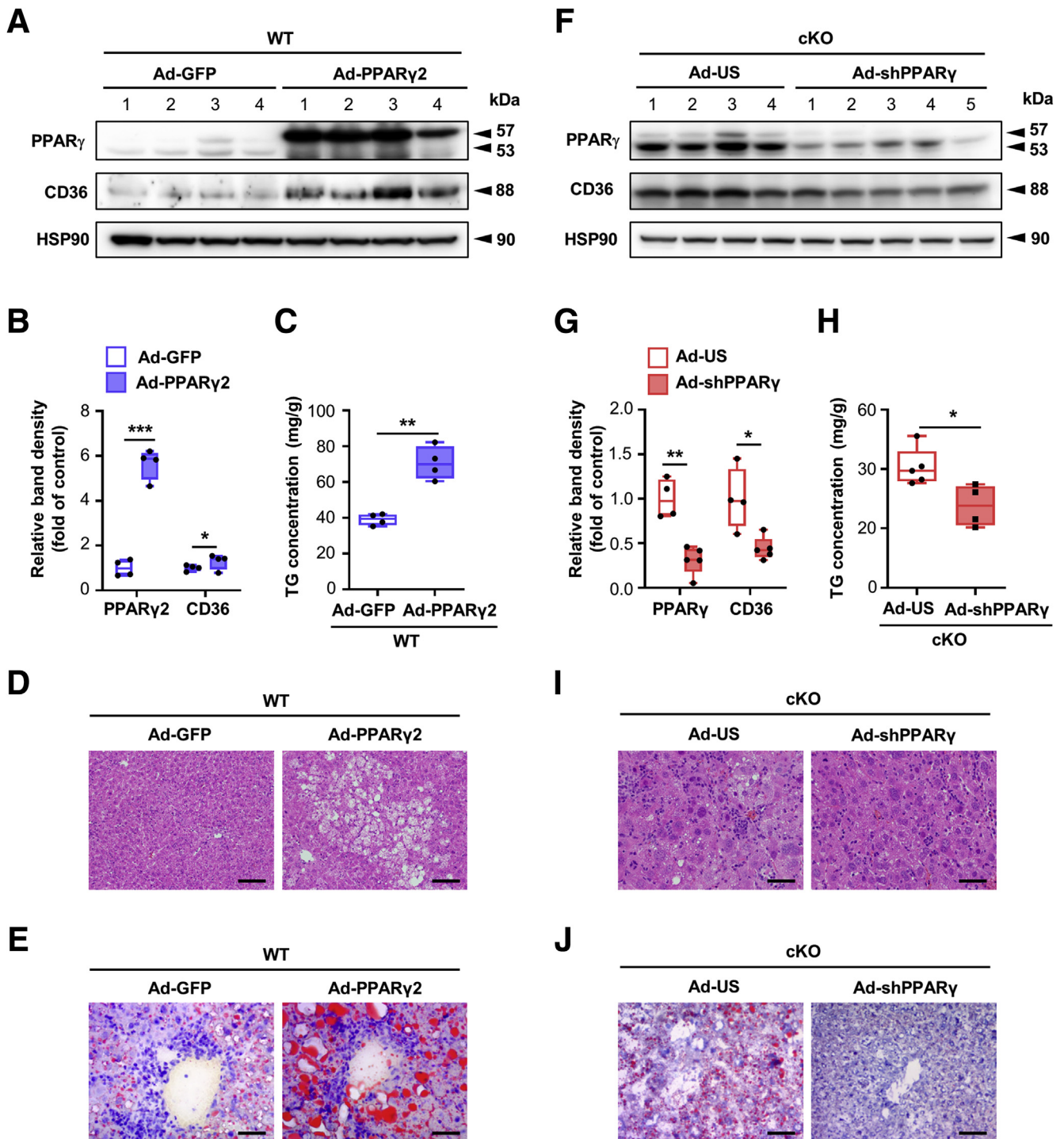


Figure 15. Effect of overexpression and knockdown of PPAR γ in hepatic steatosis. (A–E) WT mice were injected with adenovirus expressing control (Ad-GFP) or PPAR γ 2 (Ad-PPAR γ 2) 7 days before death (n = 4 per group). (A) Western blot analysis of PPAR γ , CD36, and HSP90 proteins. (B) The band densities of the proteins in panel A were quantified and presented as box plots (n = 4 per group). (C) TG levels in livers (n = 4 per group). (D and E) Representative images of histologic liver sections stained with (D) H&E and (E) Oil Red O. Scale bars: 50 μ m (D) and 200 μ m (E). (F–J) CTCF cKO mice were injected with adenovirus expressing control (Ad-US) or PPAR γ short hairpin RNA (Ad-shPPAR γ) 7 days before death (n = 4–5 per group). (F) Western blot analysis of PPAR γ , CD36, and HSP90 proteins. (G) The band densities of the proteins in panel F were quantified and presented as box plots (n = 4–5 per group). (H) TG levels in livers (n = 4 per group). (I and J) Representative images of histologic liver sections stained with (I) H&E and (J) Oil Red O. Scale bar: 50 μ m (I) and 200 μ m (J). * P < .05, ** P < .01, *** P < .001, unpaired 2-tailed Student t test.

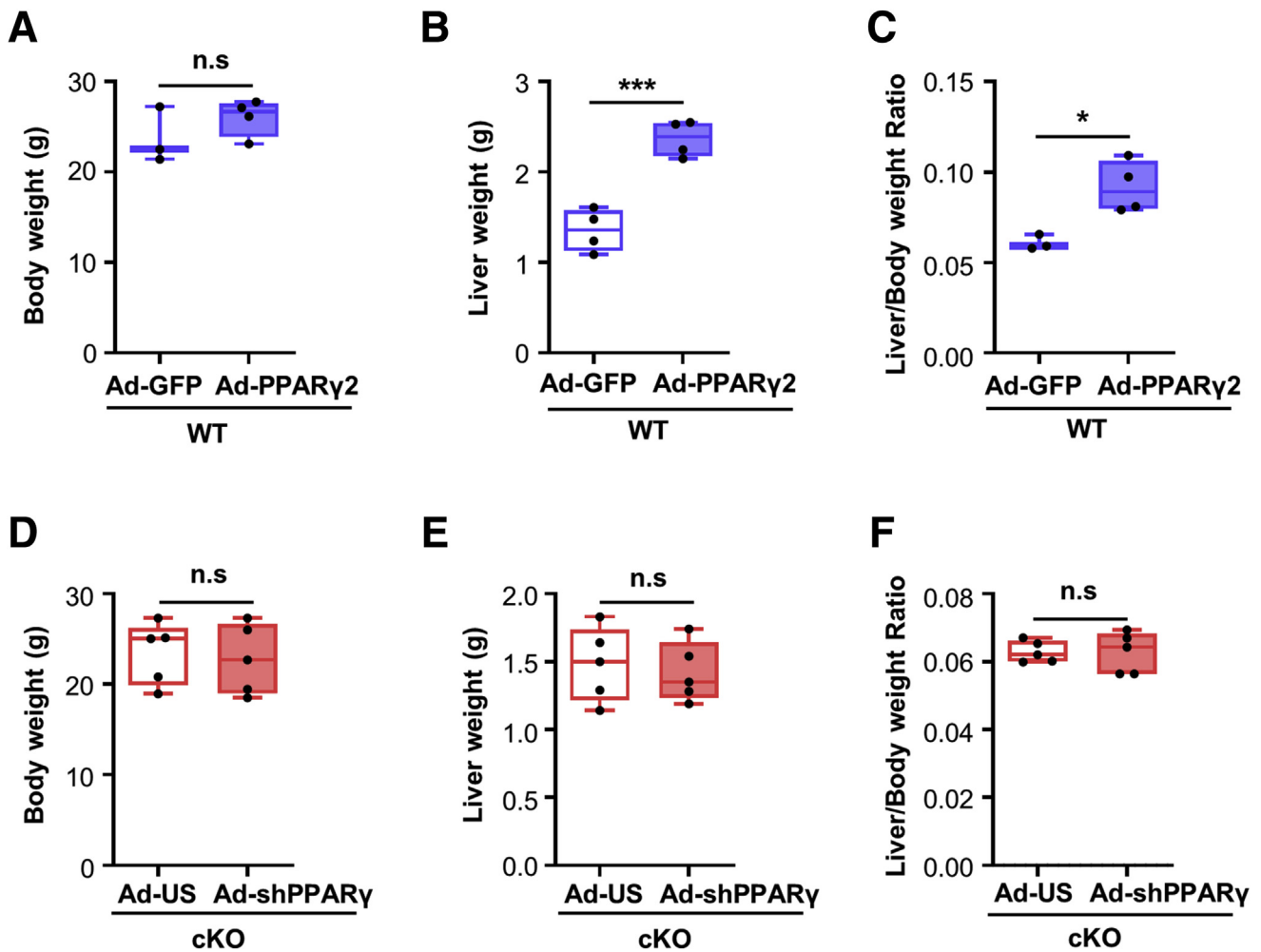


Figure 16. Effect of overexpression and knockdown of PPAR γ in body and liver weight. (A) Body weight, (B) liver weight, and (C) liver/body weight ratio of WT mice injected with adenovirus expressing control (Ad-GFP) or PPAR γ (Ad-PPAR γ 2) 7 days before death ($n = 4$ per group). (D) Body weight, (E) liver weight, and (F) liver/body weight ratio of cKO mice injected with adenovirus expressing control (Ad-US) or PPAR γ short hairpin RNA (Ad-shPPAR γ) 7 days before death ($n = 4$ –5 per group). * $P < .05$, *** $P < .001$, unpaired 2-tailed Student t test.

liver tissues were dehydrated, embedded in paraffin, sectioned at 5 μ m, and stained with H&E. For visualizing lipid deposits, liver tissues were embedded in optimal cutting temperature compound (OCT) (Sakura Finetek, Torrance, CA) and frozen on dry ice, after which 10- μ m sections were stained with Oil Red O (Sigma-Aldrich, St.Louis, MO).

Metabolic Analysis

Serum levels of alanine aminotransferase, aspartate aminotransferase, total cholesterol, and triglycerides were monitored by standard clinical chemistry assays on an automatic chemistry analyzer (7020; Hitachi, Tokyo, Japan). Hepatic lipids were extracted using a chloroform/methanol mix (2:1, vol/vol), as described previously,⁵⁴ and total cholesterol and triglyceride levels in the liver were measured using cholesterol/cholesteryl ester assay kits (Abcam, Cambridge, United Kingdom) and triglyceride assay kits (Abcam, Cambridge, United Kingdom), respectively. The

levels of free fatty acids in the liver were analyzed with gas chromatography–triple quadrupole tandem mass spectrometry. To measure Very-low-density lipoprotein (VLDL)-TG secretion rates, mice were fasted for 16 hours, pre-bled by retro-orbital bleeding, and administered intravenous injections of 10% tyloxapol (Triton WR-1339, 500 mg/kg body weight; Sigma-Aldrich, St.Louis, MO). Plasma samples were drawn serially at 0, 60, and 120 minutes after injection, and plasma TG levels were measured using triglyceride assay kits (Abcam, Cambridge, United Kingdom).

Tolerance tests

Glucose, insulin and pyruvate tolerance tests were performed as described previously.⁵⁵ Mice fasted for either 18 or 6 hours before the tolerance tests, respectively. Mice were injected intraperitoneally with either 1.5 g/kg of glucose (Sigma-Aldrich, St.Louis, MO, USA), 0.75 U/kg of insulin (regular humulin; Eli Lilly and Company,

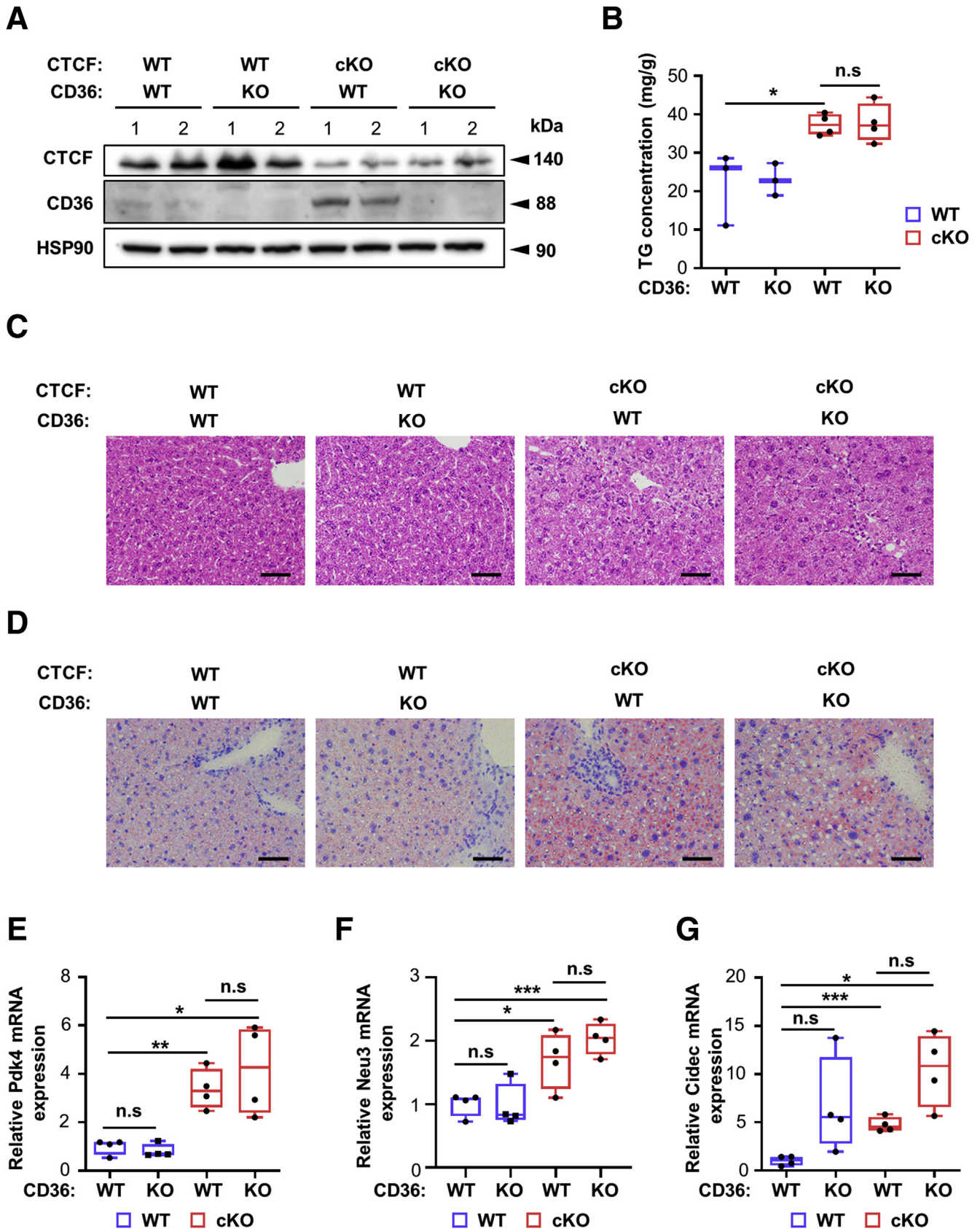


Figure 17. CD36 knockout is not enough to rescue hepatic steatosis in CTCF-deficient mice. (A) Western blot analysis of CTCF, CD36, and HSP90 proteins. (B) TG levels in livers (n = 4 per group). (C and D) Representative images of histologic liver sections stained with (C) H&E and (D) Oil Red O. Scale bar: 50 μ m. (E–G) Expression of (E) *PDK4*, (F) *NEU3*, and (G) cell death-inducing DFFA-like effector c (CIDEC) mRNA (n = 4 per group) in the livers from mice with the indicated genotype was determined by real-time qRT-PCR. **P* < .05, ***P* < .01, ****P* < .001, unpaired 2-tailed Student *t* test.

Indianapolis, IN) or 1.5g/kg of pyruvate (Sigma-Aldrich, St. Louis, MO, USA), respectively. Glucose measurements were taken up to 4 to 6 hours after injection using a glucometer (ACCU-CHEK, Active/Blood Glucose Meter/Blood Glucose Monitors; Roche Applied Science, Grenzachstrasse, Basel, Switzerland).

Immunohistochemistry and Immunofluorescence

Liver samples were fixed in 4% paraformaldehyde at room temperature, dehydrated, and embedded in paraffin. After blocking with Protein Block (Agilent Technologies DAKO, Santa Clara, CA), the sections (5 μ m) were labeled with corresponding primary antibody at 4°C overnight and horseradish-peroxidase-conjugated secondary antibody (Agilent Technologies DAKO, Santa Clara, CA) for 15 minutes at room temperature. For immunohistochemistry, detection was developed with 3,3'-diaminobenzidine substrate (Agilent Technologies DAKO, Santa Clara, CA). For detection of apoptotic cells, sections were stained with anti-cleaved caspase-3 antibodies. Cycling cells were detected by injecting the mice intraperitoneally with 200 μ g/g of BrdU in phosphate-buffered saline 4 hours before they were killed. BrdU was detected using anti-BrdU antibodies. For immunofluorescence, Alexa fluorescently labeled secondary antibodies were used at a 1:300 dilution. Nuclear DNA was counterstained with VECTASHIELD Hardset Antifade Mounting Medium (Vector Laboratories, Burlingame, CA) with 4',6-diamidino-2-phenylindole. Immunofluorescence images were generated with a LSM 700 confocal microscope (Carl Zeiss, Oberkochen, Germany) and analyzed with ZEN software (Carl Zeiss, Oberkochen, Germany). The antibodies and reagents used are listed in [Table 1](#).

Flow Cytometry

For determination of intracellular ROS, primary hepatocytes were isolated using the collagenase perfusion method as described previously⁵⁶ and were incubated with 1 μ mol/LM 5-(and-6)-carboxy-2',7'-dichlorofluorescein diacetate (Molecular Probes, Eugene, OR) diluted in phosphate-buffered saline for 30 minutes at 37°C in the dark, followed by extensive washing with phosphate-buffered saline. For measuring Kupffer cells, stained cells with anti-F4/80 antibodies were acquired using a FACSVerser or LSRFortessa flow cytometer (BD Biosciences, Franklin Lakes, NJ). TNF and IL1 β in plasma were quantified using Cytometric Bead Array Flex Sets (BD Biosciences, Franklin Lakes, NJ). All flow cytometry data were analyzed with FlowJo software (Tree Star, Woodburn, OR).

Fatty Acid Uptake Assay

Fatty acid uptake in primary hepatocytes was determined using a free fatty acid assay kit (Abcam). Primary hepatocytes were serum-deprived for 1 hour at 37°C and incubated with a fatty acid mixture for 30 minutes. Fluorescent dyes for detecting intracellular fatty acid were measured using flow cytometry.

qRT-PCR

Total RNA was isolated from liver samples using Hybrid-R Total RNA kits (GeneAll Biotechnology, Seoul, Korea). Complementary DNA was synthesized using PrimeScript RT Master Mix (Takara Bio, Shiga, Japan). Quantitative real-time PCR was performed with the ABI Quant studio real-time PCR system (Applied Biosystems, Waltham, MA), monitoring the synthesis of double-stranded DNA using SYBR Green (Qiagen, Hilden, Germany). For each sample, duplicate test reactions were analyzed to assess the expression of genes of interest, and results were normalized to Rpl7 mRNA. The sequences of the indicated primers are presented in [Table 2](#).

Western Blot

Liver tissue specimens or primary hepatocytes were lysed in T-PER Tissue Protein Extraction Reagent (Thermo Fisher Scientific, Waltham, MA) and a protease and phosphate inhibitor cocktail (Thermo Fisher Scientific, Waltham, MA). Proteins were separated on sodium dodecyl sulfate-polyacrylamide gel electrophoresis and transferred onto a polyvinylidene fluoride membrane. After blocking with 5% skim milk, the membrane was incubated with primary antibodies, followed by incubation with horseradish peroxidase-conjugated secondary antibody. Target proteins were visualized using Super Signal West Pico Chemiluminescent Substrate and Image Quant LAS 4000 (GE Healthcare, Chicago, IL). The antibodies and reagents used are listed in [Table 1](#).

Nuclear and Cytoplasmic Extraction

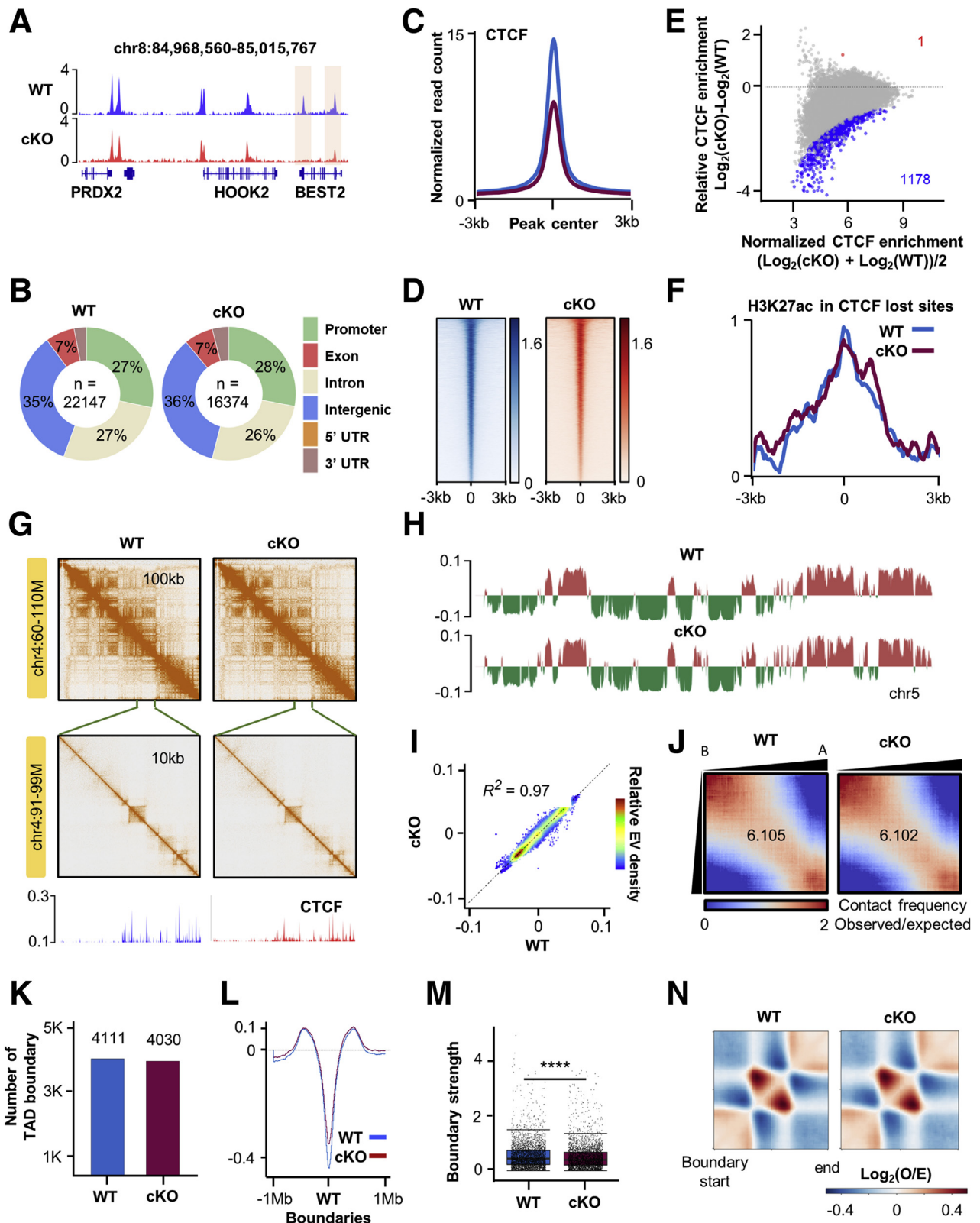
Nuclear and cytoplasmic extracts were separated according to the manufacturer's instructions for the Cell Fractionation Kit (Cell Signaling Technology, Danvers, MA).

RNA-seq

RNA-seq libraries were prepared using TruSeq RNA Sample Prep Kits (Illumina, San Diego, CA). Library quality and quantity were assessed on a bioanalyzer (Agilent Technologies DAKO) and Qubit (Invitrogen, Waltham, MA), respectively. Libraries were sequenced on the Illumina HiSeq 2500 system, generating 100-bp, paired-end reads. Reads were quality-trimmed and filtered using the NGS QC Toolkit (version 2.358; National Institute of Plant Genome research, New Delhi, Delhi, India)⁵⁷ to remove reads with low-quality bases (quality score, >20). High-quality reads were aligned to the mm10 mouse genome using STAR (version 2.5.3a; Cold Spring Harbor Laboratory, Cold Spring Harbor, NY)⁵⁸ with the following parameters: `-sjdbOverhang 100 -twopassMode Basic -outSAMtype BAM SortedByCoordinate Unsorted -chimSegmentMin 20`, with gene annotation from Ensembl (version 90; European Molecular Biology Laboratory's European Bioinformatics Institute, Hinxton, Cambridge, United Kingdom). Gene expression was quantified using RSEM (version 1.2.31; University of Wisconsin-Madison, Madison, WI),⁵⁹ and differentially expressed genes were identified using DESeq2 (version

1.18.1; Harvard School of Public Health, Boston, MA).⁶⁰ Gene ontology and pathway enrichment analyses were performed using the DAVID database (Frederick National Laboratory,

Frederick, MD).^{61,62} Gene set enrichment analysis was performed with the Broad Institute GSEA software (v4.1.0; Broad Institute, Cambridge, MA)^{63,64}



ChIP-seq

ChIP assays were performed as described previously⁶⁵ with minor modifications. Chromatin samples were immunoprecipitated with antibodies listed in Table 1. ChIP-seq libraries were prepared using a Nextera DNA Sample Prep Kit (Illumina, San Diego, CA) as described previously.⁶⁶ Libraries were sequenced on an Illumina HiSeq 2500 system, generating 101-bp, paired-end reads. Reads were quality-trimmed and filtered using Trim Galore (version 0.5.0; Babraham Bioinformatics, Cambridge, UK) to remove reads with low-quality bases (quality score, >5). High-quality reads were aligned to the mm10 mouse genome using BWA-mem (version 0.7.21; Wellcome Sanger Institute, Hinxton, Cambridge, United Kingdom)⁶⁷ with default settings. The aligned files were sorted and deduplicated for PCR duplicates using PICARD (version 1.77; Broad Institute, Cambridge, MA) (<http://broadinstitute.github.io/picard>). ChIP-seq peaks for PPAR γ and CTCF were called using MACS2⁶⁸ with the parameter BAMPE -nomodel -q 0.001. H3K27ac peaks were called using MACS2 (version 2.1.2; Harvard School of Public Health, Boston, MA) with the following parameters: -broad -extsize -shift -broad-cut-off 0.1. Enrichment of transcription factor motifs within differentially acetylated regions was assessed using HOMER *findMotifsgenome* (version 4.10; Benner Lab, University of California, San Diego, CA) with default parameters.⁶⁹ Genes with ChIP-seq peaks were annotated using HOMER *annotatePeaks* (version 4.10; Benner Lab, University of California, San Diego, CA) with the reference genome mm10. Differential enrichment of ChIP-seq peaks for H3K27ac, PPAR γ , and CTCF was analyzed using DiffBind (version 2.6.6; Cambridge Research Institute, Cambridge, United Kingdom).⁷⁰ Normalized signals for ChIP-seq data were visualized using the Integrative Genomics Viewer (Broad Institute, Cambridge, MA).⁷¹

In Situ Hi-C

In situ Hi-C was performed as previously described.⁷² In brief, liver samples were harvested, flash-frozen in liquid nitrogen, and pulverized before 1% formaldehyde cross-linking for 20 minutes and subsequent quenching with 0.125 mol/L glycine. Liver nuclei were isolated using a sucrose cushion after cross-linked tissues were thawed and dissociated using a gentleMACS Tissue Dissociator (Miltenyi Biotec, Bergisch Gladbach, Germany). Chromatin was digested using DpnII restriction enzyme (New England Biolabs, Ipswich, MA), followed by biotin incorporation with Biotin-14-Deoxyadenosine triphosphate (dATP) (Jena

Table 1. Antibodies and Reagents Used in the Study

Reagent or resource	Source	Identifier
BrdU	Invitrogen	#033900
Cleaved caspase-3	Cell Signaling Technology	#9664
F4/80	Abcam	Ab6640
F4/80	eBioscience (San Diego, CA)	#51-4801-80
HNF4 α	Abcam	Ab41898
PPAR α	Santa Cruz Biotechnology (Dallas, TX)	sc-398394
PPAR γ	Cell Signaling Technology	#2443
CD36	Novus Biologicals (Centennial, CO)	NB400-144
CTCF	Cell Signaling Technology	#2899
α -tubulin	Santa Cruz Biotechnology	sc-32293
HSP 90 α/β	Santa Cruz Biotechnology	sc-13119
Lamin B1	Abcam	Ab133741
DAPI	Vector Laboratories (Burlingame, CA)	H-1500
DCFDA	Invitrogen	C6827
CD36	BioLegend (San Diego, CA)	#102612
CD45.2	eBioscience	#47-0454-82

DAPI, 4',6-diamidino-2-phenylindole; DCFDA, 2',7'-dichlorofluorescein diacetate.

bioscience, Löbstedter Str. 71, 07749 Jena, Germany). After de-cross-linking, ligated DNA was purified and sheared to 200 to 300 bp. DNA was purified with phenol/chloroform (Sigma-Aldrich, St. Louis, MO) and quantified using Qubit dsDNA HS Assay Kits (Thermo Fisher Scientific, Waltham, MA). A total of 150 ng was used for capture with Dynabeads MyOne Streptavidin C-1 (Thermo Fisher Scientific, Waltham, MA), and an appropriate amount of Tn5 enzyme (Illumina, San Diego, CA) was added to captured DNA to generate sequencing libraries. Each library was paired-end sequenced (101 bp) on an Illumina NovaSeq6000 platform. Two biological replicates were performed in each condition.

In Situ Hi-C Data Analysis

Paired-end .fastq files from in situ Hi-C experiments were processed using HiC-Pro (version 2.11.4; Mines ParisTech, PSL-Research University, Paris, France).⁷³ Default

Figure 18. (See previous page). **Higher-order chromatin structures in WT and CTCF-deficient liver.** (A) Snapshot of ChIP-seq signal tracks for CTCF. (B) Pie charts showing the total numbers and genomic distributions of CTCF peaks identified from WT and cKO livers. (C) Histogram showing the average tag density of CTCF ChIP-seq peaks. (D) Heatmap of ChIP-Seq signals called for CTCF. (E) MA plot showing differential enrichment of CTCF between WT and cKO livers. (F) Histogram showing the average tag density of H3K27ac ChIP-seq signals at CTCF peaks lost in cKO, compared with WT (n = 1178). (G) In situ Hi-C contact maps at 100-kb and 10-kb resolution. ChIP-seq signal tracks for CTCF were aligned below the contact maps at 10-kb resolution. (H) Distributions of cis eigenvector 1 values across the entirety of chromosome 5. (I) Scatterplot shows that CTCF depletion does not affect genome-wide cis eigenvector 1 values. (J) Saddle plots representing compartmentalization strength in WT and cKO livers. (K) Number of TAD boundaries obtained with in situ Hi-C data. (L) Genome-wide averaged insulation scores plotted vs distance around insulation centers at WT TAD boundaries. (M) Boxplot shows the TAD boundary strength in WT and cKO livers. (N) Heatmaps show the average observed/expected Hi-C interactions in TAD regions. UTR, untranslated region. **** $P < .0001$, unpaired 2-tailed Student *t* test

Table 2. Primers for qRT-PCR

Primer symbols	Primer sequence, 5'-3'	
	Forward	Reverse
Ctcf	GTGGCCAAATTTTCATTGTCC	TGCTGGATGAGAGCATATCG
Tnf α	ATGTCCATTCTGAGTTCTG	AATCTGGAAAGGTCTGAAGG
Il1 β	GAGTGTGGATCCCAAGCAAT	TACCAGTTGGGGAAGCTCTGC
Il6	CCGGAGAGGAGACTTCACAG	TTGCCATTGCACAAGCTTTT
Ppar γ	CGAGTCTGTGGGGATAAAGC	GGATCCGGCAGTTAAGATCA
Ppar α	ATGCCAGTACTGCCGTTTTTC	CCGAATCTTTCAGGTCGTGT
Hnf4 α	TCTGCGAACTCCTTCTGGAT	AGGAGCAGCACGTCCTTAAA
Cd36	GCTTGCAACTGTCAGCACAT	GCCTTGCTGTAGCCAAGAAC
Pdk4	GCTTGCCAAATTTCTCGTCTC	CCTGCTTGGGATACACCAGT
Neu3	TCCAGGGGGACATTCTAACA	GCTCTGAGCCTCCCCTAGAT
Cidec	TGACCTGCACTGCTACAAGG	ATGTAGCTGGAGGTGCCAAG
Rpl7	ATGTGCCCGCAGAACCAA	GACGAAGGAGCTGCAGAACCT

settings were used to align reads to the mm10 mouse genome, remove duplicate reads, assign reads to DpnII restriction fragments, filter for valid interactions, and generate binned interaction matrices. After confirmation of good reproducibility between biological replicates using HiC-Spector, the replicate data were merged for reprocessing as combined results.⁷⁴ The validated contact pairs were transformed to Juicer hic files with hicpro2juicebox (Mines ParisTech, PSL-Research University, Paris, France). To segregate A and B compartments, the eigenvector of each chromosome of each sample was generated from the Hi-C data using the Juicer tool eigenvector command with Knight-Ruiz (KR) normalization at 100-kb resolution (version 1.22.01; (Aiden Lab, Houston, TX)).⁷⁵ The Juicer hic files were converted to .cool files using hic2cool with default parameters. Saddle plots were yielded at 100-kb resolution using cooltools (version 0.3.2; University of Edinburgh, Edinburgh, United Kingdom), and the strength of compartmentalization was defined as a ratio of (A-A + B-B)/(A-B + B-A) interactions. To identify topological domain boundaries following an insulation square analysis,⁷⁶ contact matrix files were generated from Hi-C data and subjected to calculation of insulation scores using matrix2insulation.pl (DEKKER LAB, Worcester, MA) with parameters -b 500,000 -ids 200,000 -im mean -bmoe 3 -nt 0.1. Intra-TAD DNA interactions represented as TAD strengths were determined using FAN-C with parameters -tad-strength (version 0.9.10; Max Planck Institute for Molecular Biomedicine, Muenster, Germany).⁷⁷

Data Access

Raw and processed sequencing data were deposited with Gene Expression Omnibus under the accession number GSE151503.

Statistical Analysis

Data were analyzed with an unpaired Student 2-tailed t-test using Prism software (GraphPad Software, Inc, San

Diego, CA). Errors bars plotted on graphs are presented as the means \pm SD. The upper and lower hinges of the box-and-whisker plots represent the 75th and 25th percentile, respectively. All *P* values less than .05 were considered statistically significant.

References

1. Younossi Z, Anstee QM, Marietti M, Hardy T, Henry L, Eslam M, George J, Bugianesi E. Global burden of NAFLD and NASH: trends, predictions, risk factors and prevention. *Nat Rev Gastroenterol Hepatol* 2018; 15:11–20.
2. Merckenschlager M, Nora EP. CTCF and cohesin in genome folding and transcriptional gene regulation. *Annu Rev Genomics Hum Genet* 2016;17:17–43.
3. Rowley MJ, Corces VG. Organizational principles of 3D genome architecture. *Nat Rev Genet* 2018;19:789–800.
4. Kim TG, Kim M, Lee JJ, Kim SH, Je JH, Lee Y, Song MJ, Choi Y, Chung YW, Park CG, Cho JW, Lee MG, Lee YS, Kim HP. CCCTC-binding factor controls the homeostatic maintenance and migration of Langerhans cells. *J Allergy Clin Immunol* 2015;136:713–724.
5. Gomez-Velazquez M, Badia-Careaga C, Lechuga-Vieco AV, Nieto-Arellano R, Tena JJ, Rollan I, Alvarez A, Torroja C, Caceres EF, Roy AR, Galjart N, Delgado-Olguin P, Sanchez-Cabo F, Enriquez JA, Gomez-Skarmeta JL, Manzanares M. CTCF counter-regulates cardiomyocyte development and maturation programs in the embryonic heart. *PLoS Genet* 2017;13:e1006985.
6. Shin JO, Lee JJ, Kim M, Chung YW, Min H, Kim JY, Kim HP, Bok J. CTCF regulates otic neurogenesis via histone modification in the neurog1 locus. *Mol Cells* 2018;41:695–702.
7. Soshnikova N, Montavon T, Leleu M, Galjart N, Duboule D. Functional analysis of CTCF during mammalian limb development. *Dev Cell* 2010; 19:819–830.
8. Christov M, Clark AR, Corbin B, Hakroush S, Rhee EP, Saito H, Brooks D, Hesse E, Bouxsein M, Galjart N,

- Jung JY, Mundel P, Juppner H, Weins A, Greka A. Inducible podocyte-specific deletion of CTCF drives progressive kidney disease and bone abnormalities. *JCI Insight* 2018;3:e95091.
9. Wan LB, Pan H, Hannehalli S, Cheng Y, Ma J, Fedoriw A, Lobanenkov V, Latham KE, Schultz RM, Bartolomei MS. Maternal depletion of CTCF reveals multiple functions during oocyte and preimplantation embryo development. *Development* 2008;135:2729–2738.
 10. Sams DS, Nardone S, Getselter D, Raz D, Tal M, Rayi PR, Kaphzan H, Hakim O, Elliott E. Neuronal CTCF is necessary for basal and experience-dependent gene regulation, memory formation, and genomic structure of BDNF and Arc. *Cell Rep* 2016;17:2418–2430.
 11. Li T, Lu Z, Lu L. Regulation of eye development by transcription control of CCCTC binding factor (CTCF). *J Biol Chem* 2004;279:27575–27583.
 12. Beagan JA, Duong MT, Titus KR, Zhou L, Cao Z, Ma J, Lachanski CV, Gillis DR, Phillips-Cremens JE. YY1 and CTCF orchestrate a 3D chromatin looping switch during early neural lineage commitment. *Genome Res* 2017;27:1139–1152.
 13. Marra F, Svegliati-Baroni G. Lipotoxicity and the gut-liver axis in NASH pathogenesis. *J Hepatol* 2018;68:280–295.
 14. Liu J, Li D, Zhang T, Tong Q, Ye RD, Lin L. SIRT3 protects hepatocytes from oxidative injury by enhancing ROS scavenging and mitochondrial integrity. *Cell Death Dis* 2017;8:e3158.
 15. Lee YJ, Ko EH, Kim JE, Kim E, Lee H, Choi H, Yu JH, Kim HJ, Seong JK, Kim KS, Kim JW. Nuclear receptor PPARgamma-regulated monoacylglycerol O-acyltransferase 1 (MGAT1) expression is responsible for the lipid accumulation in diet-induced hepatic steatosis. *Proc Natl Acad Sci U S A* 2012;109:13656–13661.
 16. Han L, Shen WJ, Bittner S, Kraemer FB, Azhar S. PPARs: regulators of metabolism and as therapeutic targets in cardiovascular disease. Part II: PPAR-beta/delta and PPAR-gamma. *Future Cardiol* 2017;13:279–296.
 17. Zhang C, Luo X, Chen J, Zhou B, Yang M, Liu R, Liu D, Gu HF, Zhu Z, Zheng H, Li L, Yang G. Osteoprotegerin promotes liver steatosis by targeting the ERK-PPAR-gamma-CD36 pathway. *Diabetes* 2019;68:1902–1914.
 18. Moran-Salvador E, Lopez-Parra M, Garcia-Alonso V, Titos E, Martinez-Clemente M, Gonzalez-Periz A, Lopez-Vicario C, Barak Y, Arroyo V, Claria J. Role for PPARgamma in obesity-induced hepatic steatosis as determined by hepatocyte- and macrophage-specific conditional knockouts. *FASEB J* 2011;25:2538–2550.
 19. Inoue M, Ohtake T, Motomura W, Takahashi N, Hosoki Y, Miyoshi S, Suzuki Y, Saito H, Kohgo Y, Okumura T. Increased expression of PPARgamma in high fat diet-induced liver steatosis in mice. *Biochem Biophys Res Commun* 2005;336:215–222.
 20. Gavrilova O, Haluzik M, Matsusue K, Cutson JJ, Johnson L, Dietz KR, Nicol CJ, Vinson C, Gonzalez FJ, Reitman ML. Liver peroxisome proliferator-activated receptor gamma contributes to hepatic steatosis, triglyceride clearance, and regulation of body fat mass. *J Biol Chem* 2003;278:34268–34276.
 21. Hauser S, Adelmant G, Sarraf P, Wright HM, Mueller E, Spiegelman BM. Degradation of the peroxisome proliferator-activated receptor gamma is linked to ligand-dependent activation. *J Biol Chem* 2000;275:18527–18533.
 22. Pascual G, Fong AL, Ogawa S, Gamliel A, Li AC, Perissi V, Rose DW, Willson TM, Rosenfeld MG, Glass CK. A SUMOylation-dependent pathway mediates transrepression of inflammatory response genes by PPAR-gamma. *Nature* 2005;437:759–763.
 23. Taylor J, Fischer A. Endothelial cells dictate cardiac fuel source. *Aging (Albany NY)* 2019;11:1083–1084.
 24. Verpoorten S, Sfyri P, Scully D, Mitchell R, Tzimou A, Mougios V, Patel K, Matsakas A. Loss of CD36 protects against diet-induced obesity but results in impaired muscle stem cell function, delayed muscle regeneration and hepatic steatosis. *Acta Physiol (Oxf)* 2020;228:e13395.
 25. Abumrad NA, Goldberg IJ. CD36 actions in the heart: Lipids, calcium, inflammation, repair and more? *Biochim Biophys Acta* 2016;1861:1442–1449.
 26. Glatz JFC, Luiken J. Dynamic role of the transmembrane glycoprotein CD36 (SR-B2) in cellular fatty acid uptake and utilization. *J Lipid Res* 2018;59:1084–1093.
 27. Aouadi M, Vangala P, Yawe JC, Tencerova M, Nicoloso SM, Cohen JL, Shen Y, Czech MP. Lipid storage by adipose tissue macrophages regulates systemic glucose tolerance. *Am J Physiol Endocrinol Metab* 2014;307:E374–E383.
 28. Cifarelli V, Abumrad NA. Intestinal CD36 and other key proteins of lipid utilization: role in absorption and gut homeostasis. *Compr Physiol* 2018;8:493–507.
 29. Alkhatatbeh MJ, Enjeti AK, Acharya S, Thorne RF, Lincz LF. The origin of circulating CD36 in type 2 diabetes. *Nutr Diabetes* 2013;3:e59.
 30. Miquirena-Colina ME, Lima-Cabello E, Sanchez-Campos S, Garcia-Mediavilla MV, Fernandez-Bermejo M, Lozano-Rodriguez T, Vargas-Castrillon J, Buque X, Ochoa B, Aspichueta P, Gonzalez-Gallego J, Garcia-Monzon C. Hepatic fatty acid translocase CD36 upregulation is associated with insulin resistance, hyperinsulinaemia and increased steatosis in non-alcoholic steatohepatitis and chronic hepatitis C. *Gut* 2011;60:1394–1402.
 31. Samovski D, Abumrad NA. Regulation of lipophagy in NAFLD by cellular metabolism and CD36. *J Lipid Res* 2019;60:755–757.
 32. Febbraio M, Guy E, Coburn C, Knapp FF Jr, Beets AL, Abumrad NA, Silverstein RL. The impact of over-expression and deficiency of fatty acid translocase (FAT)/CD36. *Mol Cell Biochem* 2002;239:193–197.
 33. Koonen DP, Jacobs RL, Febbraio M, Young ME, Soltys CL, Ong H, Vance DE, Dyck JR. Increased hepatic CD36 expression contributes to dyslipidemia associated with diet-induced obesity. *Diabetes* 2007;56:2863–2871.
 34. Wilson CG, Tran JL, Erion DM, Vera NB, Febbraio M, Weiss EJ. Hepatocyte-specific disruption of CD36

- attenuates fatty liver and improves insulin sensitivity in HFD-fed mice. *Endocrinology* 2016;157:570–585.
35. Brundert M, Heeren J, Merkel M, Carambia A, Herkel J, Groitl P, Dobner T, Ramakrishnan R, Moore KJ, Rinninger F. Scavenger receptor CD36 mediates uptake of high density lipoproteins in mice and by cultured cells. *J Lipid Res* 2011;52:745–758.
 36. Bujold K, Rhoads D, Jossart C, Febbraio M, Marleau S, Ong H. CD36-mediated cholesterol efflux is associated with PPARgamma activation via a MAPK-dependent COX-2 pathway in macrophages. *Cardiovasc Res* 2009;83:457–464.
 37. Zhou J, Febbraio M, Wada T, Zhai Y, Kuruba R, He J, Lee JH, Khadem S, Ren S, Li S, Silverstein RL, Xie W. Hepatic fatty acid transporter Cd36 is a common target of LXR, PXR, and PPARgamma in promoting steatosis. *Gastroenterology* 2008;134:556–567.
 38. Wilmsen HM, Ciaraldi TP, Carter L, Reehman N, Mudaliar SR, Henry RR. Thiazolidinediones upregulate impaired fatty acid uptake in skeletal muscle of type 2 diabetic subjects. *Am J Physiol Endocrinol Metab* 2003;285:E354–E362.
 39. Langhi C, Baldan A. CIDEA/FSP27 is regulated by peroxisome proliferator-activated receptor alpha and plays a critical role in fasting- and diet-induced hepato-steatosis. *Hepatology* 2015;61:1227–1238.
 40. Zhang M, Zhao Y, Li Z, Wang C. Pyruvate dehydrogenase kinase 4 mediates lipogenesis and contributes to the pathogenesis of nonalcoholic steatohepatitis. *Biochem Biophys Res Commun* 2018;495:582–586.
 41. Yoshizumi S, Suzuki S, Hirai M, Hinokio Y, Yamada T, Yamada T, Tsunoda U, Aburatani H, Yamaguchi K, Miyagi T, Oka Y. Increased hepatic expression of ganglioside-specific sialidase, NEU3, improves insulin sensitivity and glucose tolerance in mice. *Metabolism* 2007;56:420–429.
 42. Zuin J, Dixon JR, van der Reijden MI, Ye Z, Kolovos P, Brouwer RW, van de Corput MP, van de Werken HJ, Knoch TA, van IWF, Grosveld FG, Ren B, Wendt KS. Cohesin and CTCF differentially affect chromatin architecture and gene expression in human cells. *Proc Natl Acad Sci U S A* 2014;111:996–1001.
 43. Nora EP, Goloborodko A, Valton AL, Gibcus JH, Ueberohrn A, Abdennur N, Dekker J, Mirny LA, Bruneau BG. Targeted degradation of CTCF decouples local insulation of chromosome domains from genomic compartmentalization. *Cell* 2017;169:930–944 e22.
 44. Feldstein AE, Canbay A, Guicciardi ME, Higuchi H, Bronk SF, Gores GJ. Diet associated hepatic steatosis sensitizes to Fas mediated liver injury in mice. *J Hepatol* 2003;39:978–983.
 45. Cheung O, Sanyal AJ. Abnormalities of lipid metabolism in nonalcoholic fatty liver disease. *Semin Liver Dis* 2008;28:351–359.
 46. Nolan CJ, Larter CZ. Lipotoxicity: why do saturated fatty acids cause and monounsaturates protect against it? *J Gastroenterol Hepatol* 2009;24:703–706.
 47. Anderson N, Borlak J. Molecular mechanisms and therapeutic targets in steatosis and steatohepatitis. *Pharmacol Rev* 2008;60:311–357.
 48. Garbarino J, Sturley SL. Saturated with fat: new perspectives on lipotoxicity. *Curr Opin Clin Nutr Metab Care* 2009;12:110–116.
 49. Postic C, Shiota M, Niswender KD, Jetton TL, Chen Y, Moates JM, Shelton KD, Lindner J, Cherrington AD, Magnuson MA. Dual roles for glucokinase in glucose homeostasis as determined by liver and pancreatic beta cell-specific gene knock-outs using Cre recombinase. *J Biol Chem* 1999;274:305–315.
 50. Febbraio M, Abumrad NA, Hajjar DP, Sharma K, Cheng W, Pearce SF, Silverstein RL. A null mutation in murine CD36 reveals an important role in fatty acid and lipoprotein metabolism. *J Biol Chem* 1999;274:19055–19062.
 51. Luo J, Deng ZL, Luo X, Tang N, Song WX, Chen J, Sharff KA, Luu HH, Haydon RC, Kinzler KW, Vogelstein B, He TC. A protocol for rapid generation of recombinant adenoviruses using the AdEasy system. *Nat Protoc* 2007;2:1236–1247.
 52. Koo SH, Flechner L, Qi L, Zhang X, Sreter RA, Jeffries S, Hedrick S, Xu W, Boussouar F, Brindle P, Takemori H, Montminy M. The CREB coactivator TORC2 is a key regulator of fasting glucose metabolism. *Nature* 2005;437:1109–1111.
 53. Herzig S, Hedrick S, Morante I, Koo SH, Galimi F, Montminy M. CREB controls hepatic lipid metabolism through nuclear hormone receptor PPAR-gamma. *Nature* 2003;426:190–193.
 54. Park S, Oh TS, Kim S, Kim EK. Palmitate-induced autophagy liberates monounsaturated fatty acids and increases Agrp expression in hypothalamic cells. *Anim Cells Syst (Seoul)* 2019;23:384–391.
 55. Ferron M, Wei J, Yoshizawa T, Del Fattore A, DePinho RA, Teti A, Ducy P, Karsenty G. Insulin signaling in osteoblasts integrates bone remodeling and energy metabolism. *Cell* 2010;142:296–308.
 56. Kim SY, Kim HI, Kim TH, Im SS, Park SK, Lee IK, Kim KS, Ahn YH. SREBP-1c mediates the insulin-dependent hepatic glucokinase expression. *J Biol Chem* 2004;279:30823–30829.
 57. Patel RK, Jain M. NGS QC Toolkit: a toolkit for quality control of next generation sequencing data. *PLoS One* 2012;7:e30619.
 58. Dobin A, Davis CA, Schlesinger F, Drenkow J, Zaleski C, Jha S, Batut P, Chaisson M, Gingeras TR. STAR: ultrafast universal RNA-seq aligner. *Bioinformatics* 2013;29:15–21.
 59. Li B, Dewey CN. RSEM: accurate transcript quantification from RNA-Seq data with or without a reference genome. *BMC Bioinformatics* 2011;12:323.
 60. Love MI, Huber W, Anders S. Moderated estimation of fold change and dispersion for RNA-seq data with DESeq2. *Genome Biol* 2014;15:550.
 61. Huang da W, Sherman BT, Lempicki RA. Systematic and integrative analysis of large gene lists using DAVID bioinformatics resources. *Nat Protoc* 2009;4:44–57.
 62. Huang da W, Sherman BT, Lempicki RA. Bioinformatics enrichment tools: paths toward the comprehensive functional analysis of large gene lists. *Nucleic Acids Res* 2009;37:1–13.

63. Subramanian A, Tamayo P, Mootha VK, Mukherjee S, Ebert BL, Gillette MA, Paulovich A, Pomeroy SL, Golub TR, Lander ES, Mesirov JP. Gene set enrichment analysis: a knowledge-based approach for interpreting genome-wide expression profiles. *Proc Natl Acad Sci U S A* 2005;102:15545–15550.
64. Mootha VK, Lindgren CM, Eriksson KF, Subramanian A, Sihag S, Lehar J, Puigserver P, Carlsson E, Ridderstrale M, Laurila E, Houstis N, Daly MJ, Patterson N, Mesirov JP, Golub TR, Tamayo P, Spiegelman B, Lander ES, Hirschhorn JN, Altshuler D, Groop LC. PGC-1 α -responsive genes involved in oxidative phosphorylation are coordinately down-regulated in human diabetes. *Nat Genet* 2003;34:267–273.
65. Park JH, Choi Y, Song MJ, Park K, Lee JJ, Kim HP. Dynamic long-range chromatin interaction controls expression of IL-21 in CD4⁺ T cells. *J Immunol* 2016;196:4378–4389.
66. Schmidl C, Rendeiro AF, Sheffield NC, Bock C. ChIPmentation: fast, robust, low-input ChIP-seq for histones and transcription factors. *Nat Methods* 2015;12:963–965.
67. Li H, Durbin R. Fast and accurate short read alignment with Burrows-Wheeler transform. *Bioinformatics* 2009;25:1754–1760.
68. Zhang Y, Liu T, Meyer CA, Eeckhoute J, Johnson DS, Bernstein BE, Nusbaum C, Myers RM, Brown M, Li W, Liu XS. Model-based analysis of ChIP-Seq (MACS). *Genome Biol* 2008;9:R137.
69. Heinz S, Benner C, Spann N, Bertolino E, Lin YC, Laslo P, Cheng JX, Murre C, Singh H, Glass CK. Simple combinations of lineage-determining transcription factors prime cis-regulatory elements required for macrophage and B cell identities. *Mol Cell* 2010;38:576–589.
70. Ross-Innes CS, Stark R, Teschendorff AE, Holmes KA, Ali HR, Dunning MJ, Brown GD, Gojis O, Ellis IO, Green AR, Ali S, Chin SF, Palmieri C, Caldas C, Carroll JS. Differential oestrogen receptor binding is associated with clinical outcome in breast cancer. *Nature* 2012;481:389–393.
71. Robinson JT, Thorvaldsdottir H, Winckler W, Guttman M, Lander ES, Getz G, Mesirov JP. Integrative genomics viewer. *Nat Biotechnol* 2011;29:24–26.
72. Rao SS, Huntley MH, Durand NC, Stamenova EK, Bochkov ID, Robinson JT, Sanborn AL, Machol I, Omer AD, Lander ES, Aiden EL. A 3D map of the human genome at kilobase resolution reveals principles of chromatin looping. *Cell* 2014;159:1665–1680.
73. Servant N, Varoquaux N, Lajoie BR, Viara E, Chen CJ, Vert JP, Heard E, Dekker J, Barillot E. HiC-Pro: an optimized and flexible pipeline for Hi-C data processing. *Genome Biol* 2015;16:259.
74. Yan KK, Yardimci GG, Yan C, Noble WS, Gerstein M. HiC-spector: a matrix library for spectral and reproducibility analysis of Hi-C contact maps. *Bioinformatics* 2017;33:2199–2201.
75. Durand NC, Shamim MS, Machol I, Rao SS, Huntley MH, Lander ES, Aiden EL. Juicer provides a one-click system for analyzing loop-resolution Hi-C experiments. *Cell Syst* 2016;3:95–98.
76. Crane E, Bian Q, McCord RP, Lajoie BR, Wheeler BS, Ralston EJ, Uzawa S, Dekker J, Meyer BJ. Condensin-driven remodelling of X chromosome topology during dosage compensation. *Nature* 2015;523:240–244.
77. Kruse K, Hug CB, Vaquerizas JM, FAN -C. a feature-rich framework for the analysis and visualisation of chromosome conformation capture data. *Genome Biol* 2020;21:303.

Received July 24, 2020. Accepted July 27, 2021.

Correspondence

Address correspondence to: Hyoung-Pyo Kim, PhD, Department of Environmental Medical Biology, Institute of Tropical Medicine, Yonsei University College of Medicine, 50-1 Yonsei-ro, Seodaemun-gu, Seoul 03722, Korea. e-mail: kimhp@yuhs.ac; fax: (82) 2-363-8676.

CRedit Authorship Contributions

Yeeun Choi (Conceptualization: Supporting; Data curation: Lead; Formal analysis: Lead; Investigation: Lead; Writing – original draft: Supporting)
 Min-Ji Song (Conceptualization: Supporting; Data curation: Equal; Formal analysis: Equal; Investigation: Equal; Writing – original draft: Supporting)
 Woong-Jae Jung (Data curation: Equal; Formal analysis: Equal)
 Haengdueng Jeong (Investigation: Supporting)
 Seokjae Park (Formal analysis: Supporting)
 Bobae Yang (Formal analysis: Supporting)
 Eun-Chong Lee (Formal analysis: Supporting)
 Jung-Sik Joo (Formal analysis: Supporting)
 Dahee Choi (Resources: Supporting)
 Seung-Hoi Koo (Resources: Supporting)
 Eun-Kyoung Kim (Data curation: Supporting)
 Ki Taek Nam (Conceptualization: Supporting; Data curation: Supporting; Formal analysis: Supporting; Investigation: Supporting)
 Hyoung-Pyo Kim (Conceptualization: Lead; Funding acquisition: Lead; Project administration: Lead; Supervision: Lead; Writing – original draft: Lead)

Conflicts of interest

The authors disclose no conflicts.

Funding

This work was supported by National Research Foundation of Korea (NRF) grants funded by the Korean government (Ministry of Science and ICT (MSIT)) (2016R1A2B4014183, 2017M3C9A5029978, 2018M3A9D3079290, and 2020R1A2C2013258 to H.-P. Kim).